







The PHANGS-HST Survey: Physics at High Angular resolution in Nearby Galaxies with the Hubble Space Telescope

JANICE C. LEE ¹, BRADLEY C. WHITMORE,² DAVID A. THILKER ³, SINAN DEGER,¹ KIRSTEN L. LARSON,¹
LEONARDO UBEDA,² GAGANDEEP S. ANAND ⁴, MEDERIC BOQUIEN,⁵ RUPALI CHANDAR ⁶, DANIEL A. DALE ⁷,
ERIC Emsellem ^{8,9}, ADAM K. LEROY ¹⁰, ERIK ROSOLOWSKY ¹¹, EVA SCHINNERER ¹², JUDY SCHMIDT ¹³,
JORDAN TURNER ⁷, SCHUYLER VAN DYK,¹ RICHARD L. WHITE,² ASHLEY T. BARNES ¹⁴, FRANCESCO BELFIORE ¹⁵,
FRANK BIGIEL ¹⁴, GUILLERMO A. BLANC ^{16,17}, YIXIAN CAO ¹⁸, MELANIE CHEVANCE ¹⁹, ENRICO CONGIU ¹⁷,
OLEG V. EGOROV ^{19,20}, SIMON C. O. GLOVER ²¹, KATHRYN GRASHA ²², BRENT GROVES ^{23,22},
JONATHAN HENSHAW,¹² ANNIE HUGHES,^{24,25} RALF S. KLESSEN ^{21,26}, ERIC KOCH ^{27,11}, KATHRYN KRECKEL ¹⁹,
J. M. DIEDERIK KRUIJSSEN ¹⁹, DAIZHONG LIU ¹², LAURA A. LOPEZ ^{10,28}, NESS MAYKER ^{10,28},
SHARON E. MEIDT ²⁹, ERIC J. MURPHY ³⁰, HSI-AN PAN ¹², JÉRÔME PETY ^{31,32}, MIGUEL QUEREJETA ³³,
ALESSANDRO RAZZA ¹⁷, TOSHIKI SAITO ¹², PATRICIA SÁNCHEZ-BLÁZQUEZ ^{34,35}, FRANCESCO SANTORO ¹²,
AMY SARDONE ^{10,28}, FABIAN SCHEUERMANN,¹⁹ ANDREAS SCHRUBA,³⁶ JIAYI SUN ¹⁰, ANTONIO USERO ³³,
E. WATKINS,¹⁹ AND THOMAS G. WILLIAMS ¹²

¹Caltech-IPAC, 1200 E. California Blvd. Pasadena, CA 91125, USA

²Space Telescope Science Institute, 3700 San Martin Drive, Baltimore, MD 21218, USA

³Department of Physics and Astronomy, The Johns Hopkins University, Baltimore, MD 21218, USA

⁴Institute for Astronomy, University of Hawaii, 2680 Woodlawn Drive, Honolulu, HI 96822, USA

⁵Centro de Astronomía (CITEVA), Universidad de Antofagasta, Avenida Angamos 601, Antofagasta, Chile

⁶University of Toledo, 2801 W. Bancroft St., Mail Stop 111, Toledo, OH, 43606

⁷Department of Physics and Astronomy, University of Wyoming, Laramie, WY 82071, USA

⁸European Southern Observatory, Karl-Schwarzschild Straße 2, D-85748 Garching bei München, Germany

⁹Univ Lyon, Univ Lyon 1, ENS de Lyon, CNRS, Centre de Recherche Astrophysique de Lyon UMR5574,
F-69230 Saint-Genis-Laval, France

¹⁰Department of Astronomy, The Ohio State University, 140 West 18th Avenue, Columbus, Ohio 43210, USA

¹¹Department of Physics, University of Alberta, Edmonton, AB T6G 2E1, Canada

¹²Max-Planck-Institut für Astronomie, Königstuhl 17, D-69117, Heidelberg, Germany

¹³Astrophysics Source Code Library, Michigan Technological University, 1400 Townsend Drive, Houghton, MI 49931

¹⁴Argelander-Institut für Astronomie, Universität Bonn, Auf dem Hügel 71, 53121 Bonn, Germany

¹⁵INAF – Osservatorio Astrofisico di Arcetri, Largo E. Fermi 5, I-50157, Firenze, Italy

¹⁶Observatories of the Carnegie Institution for Science, 813 Santa Barbara Street, Pasadena, CA 91101, USA

¹⁷Departamento de Astronomía, Universidad de Chile, Camino del Observatorio 1515, Las Condes, Santiago, Chile

¹⁸Aix Marseille Univ, CNRS, CNES, LAM (Laboratoire d'Astrophysique de Marseille), F-13388 Marseille, France

¹⁹Astronomisches Rechen-Institut, Zentrum für Astronomie der Universität Heidelberg, Mönchhofstraße 12-14, D-69120 Heidelberg,
Germany

²⁰Sternberg Astronomical Institute, Lomonosov Moscow State University, Universitetsky pr. 13, 119234 Moscow, Russia

²¹Universität Heidelberg, Zentrum für Astronomie, Institut für Theoretische Astrophysik, Albert-Ueberle-Str 2, D-69120 Heidelberg,
Germany

²²Research School of Astronomy and Astrophysics, Australian National University, Canberra, ACT 2611, Australia

²³International Centre for Radio Astronomy Research, University of Western Australia, 35 Stirling Highway, Crawley, WA 6009,
Australia

²⁴CNRS, IRAP, 9 Av. du Colonel Roche, BP 44346, F-31028 Toulouse cedex 4, France

²⁵Université de Toulouse, UPS-OMP, IRAP, F-31028 Toulouse cedex 4, France

²⁶Universität Heidelberg, Interdisziplinäres Zentrum für Wissenschaftliches Rechnen, Im Neuenheimer Feld 205, D-69120 Heidelberg,
Germany

²⁷Harvard-Smithsonian Center for Astrophysics, 60 Garden Street, Cambridge, MA 02138, USA

²⁸Center for Cosmology and Astroparticle Physics, 191 West Woodruff Avenue, Columbus, OH 43210, USA

²⁹Sterrenkundig Observatorium, Universiteit Gent, Krijgslaan 281 S9, B-9000 Gent, Belgium

³⁰*National Radio Astronomy Observatory, 520 Edgemont Road, Charlottesville, VA 22903-2475, USA*

³¹*Institut de Radioastronomie Millimétrique (IRAM), 300 Rue de la Piscine, F-38406 Saint Martin d'Hères, France*

³²*Observatoire de Paris, PSL Research University, CNRS, Sorbonne Universités, 75014 Paris*

³³*Observatorio Astronómico Nacional (IGN), C/Alfonso XII, 3, E-28014 Madrid, Spain*

³⁴*Departamento de Física de la Tierra y Astrofísica, Universidad Complutense de Madrid, E-28040 Madrid, Spain*

³⁵*Instituto de Física de Partículas y del Cosmos, Universidad Complutense de Madrid, E-28040 Madrid, Spain*

³⁶*Max-Planck-Institut für extraterrestrische Physik, Giessenbachstraße 1, D-85748 Garching, Germany*

(Received January 11, 2021; Revised January 11, 2021; Accepted January 11, 2021)

Submitted to ApJS

ABSTRACT

The PHANGS program is building the first dataset to enable the multi-phase, multi-scale study of star formation across the nearby spiral galaxy population. This effort is enabled by large Treasury programs with ALMA, VLT/MUSE, and HST, with which we have obtained CO(2–1) imaging, optical spectroscopic mapping, and high resolution UV-optical imaging, respectively. Here, we present PHANGS-HST, which is obtaining five band NUV-U-B-V-I imaging of the disks of 38 spiral galaxies at distances of 4–23 Mpc, and parallel V and I band imaging of their halos, to provide a census of tens of thousands of compact star clusters and associations. The combination of HST, ALMA, and VLT/MUSE observations will yield an unprecedented joint catalog of the observed and physical properties of $\sim 100,000$ star clusters, associations, HII regions, and molecular clouds. With these basic units of star formation, PHANGS will systematically chart the evolutionary cycling between gas and stars, across a diversity of galactic environments found in nearby galaxies. We discuss the design of the PHANGS-HST survey, and provide an overview of the HST data processing pipeline and first results, highlighting new methods for selecting star cluster candidates, morphological classification of candidates with convolutional neural networks, and identification of stellar associations over a range of physical scales with a watershed algorithm. We describe the cross-observatory imaging, catalogs, and software products to be released, which will seed a broad range of community science, in particular, upcoming JWST study of dust embedded star formation and ISM physics.

Keywords: star formation — star clusters — spiral galaxies — surveys

1. INTRODUCTION

How do stars form from the complex multi-phase interstellar medium (ISM) in galaxies? This question lies at the heart of astrophysics, as star formation is a key process governing the evolution of baryons in the universe (Péroux & Howk 2020). Star formation converts interstellar matter into stars and their planetary systems, depletes galaxies of gas, and feeds back metals, energy, and momentum into the ISM, which may reach the halos of galaxies and beyond. In turn, this feedback, together with galactic-scale inflows and dynamics, impacts the state of the gas and the future of star formation.

The complex flow patterns within the galactic ISM determine where and at what rate stars form, and are themselves driven by the energy and momentum input from massive stars (Mac Low & Klessen 2004; McKee & Ostriker 2007; Hennebelle & Falgarone 2012; Federath 2013). Star formation typically occurs in molecular clouds (Blitz 1993; Heyer & Dame 2015; Miville-

Deschênes et al. 2017), parts of which can become gravitationally unstable and contract until new stars are born (e.g. Krumholz & McKee 2005; Dobbs et al. 2014; Chevance et al. 2020). This process is controlled by the intricate interplay between self-gravity and various opposing agents, such as supersonic turbulence, magnetic fields, radiation, and gas and cosmic ray pressure (Elmegreen 2000; McKee & Ostriker 2007; Girichidis et al. 2020). The local process of stellar birth is also impacted by the supply, organization, and stability of cloud-scale natal gas as governed by large-scale galaxy dynamics, including spiral arm features or perturbations from satellite galaxies or accretion of fresh gas from the cosmic web (see, e.g. Kennicutt 1998; Dobbs et al. 2006; Dobbs 2008; Leroy et al. 2008, 2013; Meidt et al. 2013, 2020, for further discussion). Stellar feedback, in the form of radiation, winds, and supernova explosions, creates a hierarchy of highly non-linear feedback loops that strongly influence the dynamical behavior across a wide range of physical scales (e.g. Hopkins et al. 2014; Lopez

et al. 2014; Walch et al. 2015; Gnedin 2016; Rahner et al. 2017; Olivier et al. 2020), determines the chemical and thermal state of the ISM, and affects subsequent star formation (e.g. Klessen & Glover 2016).

Decades of observations across the electromagnetic spectrum have taught us that all of these mechanisms that drive, regulate and extinguish star formation operate together over this vast range of stellar, interstellar, galactic, and circumgalactic scales. Accordingly, we have come to recognize that systematic observations – spanning key spatial scales and phases of the star formation cycle, across different galactic environments – are essential for the development of a robust, unified model of star formation and galaxy evolution.

Here, we present the PHANGS-HST Treasury survey, which as part of the Physics at High Angular Resolution in Nearby Galaxies¹ (PHANGS) program, is building a dataset for the systematic multi-scale, multi-phase study of star formation. PHANGS is charting the connections between giant molecular clouds, HII regions, and young stars throughout a diversity of galactic environments in the local universe by combining observations from new Treasury programs with ALMA, VLT/MUSE, and HST, with supporting data including ground-based H α , VLA HI, Astrosat FUV/NUV wide-field imaging, and the wealth of panchromatic ground- and space-based survey observations collected for the nearby galaxies in the sample over the past three decades. PHANGS is composed of three major components:

PHANGS-ALMA: The foundation of PHANGS has been built with the transformative capabilities of the Atacama Large Millimeter/submillimeter Array (ALMA), which are used through a Cycle 5 PHANGS-ALMA Large Program (PI E. Schinnerer) and small precursor programs to obtain $\sim 1''$ resolution CO(2–1) maps for a sample of 74 massive spiral galaxies at distances of 4–23 Mpc. At these distances, ALMA can detect individual giant molecular clouds with better than 2.4 km s^{-1} velocity resolution and physical resolutions of $\sim 50\text{--}100 \text{ pc}$, while still efficiently covering the star-forming disk (Sun et al. 2018, A. K. Leroy et al. in preparation).

PHANGS-MUSE: With the Very Large Telescope/Multi Unit Spectroscopic Explorer (VLT/MUSE), PHANGS-MUSE (PI E. Schinnerer) has obtained IFU spectroscopy with $\sim 2.5 \text{ \AA}$ spectral resolution and $\sim 0''.7$ spatial resolution for 19 of these galaxies to deliver a 3D view of the ionized (10^4 K) gas, stellar populations, and kinematics via various gas and stellar tracers in the optical from 4800–9300 \AA (E. Emsellem et al. in prepara-

tion; see first results in Kreckel et al. 2018; Ho et al. 2019; Kreckel et al. 2019, 2020). To supplement the MUSE observations, the PHANGS-H α survey (A. Razza et al. in preparation) has obtained seeing-limited ($\sim 1''$) ground-based narrow-band H α imaging, to provide star formation rate (SFR) maps and catalogs of ionized nebulae for the full PHANGS-ALMA sample. The data was obtained using WFI on the ESO/MPG 2.2m telescope at La Silla, and the DirectCCD on the du Pont 2.5m telescope at Las Campanas Observatory.

PHANGS-HST, the subject of this paper, is a Cycle 26 Hubble Space Telescope Treasury survey (PI J. C. Lee) which is obtaining *NUV-U-B-V-I* imaging of 38 galaxies from the parent PHANGS-ALMA sample, including all 19 galaxies with MUSE IFU spectroscopy.

The high-resolution capabilities of HST ($\sim 0''.08$) have enabled the study of compact star clusters and associations in galaxies out to distances of several tens of Mpc (e.g., Whitmore et al. 1999; Linden et al. 2017; Adamo et al. 2020). These structures, which typically have half-light radii of a few parsec (Portegies Zwart et al. 2010; Ryon et al. 2017; Krumholz et al. 2019), are basic units of star formation. They have been the focus of much recent work and are not only important to study in their own right (e.g., Whitmore et al. 2007; Chandar et al. 2010; Kruijssen 2012; Krumholz et al. 2019; Adamo et al. 2020), but also have great utility as ‘clocks’ – effectively single-aged stellar populations that can be age-dated and used to time various star formation and ISM processes. The PHANGS-HST UV-optical imaging will enable inventories of young star clusters and associations down to a few thousand solar masses, with age and mass determinations from SED-fitting accurate to a factor of ~ 2 (e.g. Turner et al. 2021) on average.

Altogether PHANGS will yield an unprecedented sample of $\sim 100,000$ star clusters, associations, HII regions, and molecular clouds in diverse galactic environments to provide answers to the following open questions:

- What are the timescales for the onset of star formation in clouds, the destruction of clouds, and the removal of gas from young star clusters?
- How are the mass functions of star clusters/associations related to those of clouds? What are the implied star formation efficiencies?
- How are star formation and gas organized into multi-scale structures? How do their relative spatial distributions evolve with time?

These questions, particularly those examining the relationship between molecular clouds and star clusters, have been posed in the context of the Milky Way (Mur-

¹ <http://www.phangs.org>

ray 2011; Lee et al. 2016) and selected Local Group and Nearby galaxies (e.g., M51: Hughes et al. 2013, Grasha et al. 2019; NGC7793: Grasha et al. 2018; NGC300: Kruijssen et al. 2019). But whether the answers to the questions vary with galactic environment is still unclear, as there has not yet been a systematic study on the cluster scale across a well-defined sample of galaxies spanning a broad range of global properties. PHANGS will provide not only the answers to these questions, but moreover how they depend on key galactic properties such as the phase balance and physical conditions of the ISM, stellar mass, gas mass, SFR, the surface densities of these quantities, metallicity, and the presence of dynamical features such as rings, bars, and spiral arms.

This paper presents the design of the PHANGS-HST survey, and gives an overview of the data processing pipeline developed to generate the data products required for star formation studies on parsec scales. The remainder of this paper is organized as follows. In Section 2, we describe how galaxies are selected from the parent PHANGS sample for observation with HST, and properties of the sample. HST imaging observations with WFC3 and ACS are described in Section 3. Section 4 describes the PHANGS-HST pipeline used to produce catalogs of compact star clusters and associations, and to measure their observed and physical properties. This high-level description is intended to provide the framework for a series of papers, as summarized in Section 4, which document each of the major components in detail, in particular new methods for selecting star cluster candidates, morphological classification of candidates, and identification of stellar associations over a range of physical scales. Data products resulting from this pipeline which will be released to support community science are described in Section 5.

Magnitudes in this and other PHANGS-HST pipeline papers are given in the Vega system, to facilitate comparison with prior HST studies of resolved stellar populations, unless otherwise noted.

2. GALAXY SAMPLE

Galaxies are chosen for HST observations from the PHANGS-ALMA Large Program sample (PI E. Schinnerer). PHANGS-ALMA has obtained CO(2–1) maps for a complete sample of 74 southern galaxies² ($-75^\circ < \delta < 20^\circ$; i.e. ALMA-observable), which were selected

to be massive ($M_* \gtrsim 10^{9.75} M_\odot$), star-forming, not edge-on to the line-of-sight, and at distances $\lesssim 17$ Mpc.³ CO(2–1) observations were obtained for this sample via an ALMA Cycle 5 Large Program (2017.1.00886.L), which builds upon and incorporates several smaller precursor programs in Cycles 2–3.⁴ A full description of the PHANGS-ALMA Large Program sample criteria, and derivation of integrated properties used for selection, such as stellar mass (M_*), SFR, and integrated CO luminosities, is given in A. K. Leroy et al. (in preparation).

With HST, we target the galaxies best-suited for joint HST-ALMA analysis of resolved young stellar populations and giant molecular clouds. That is, we select galaxies from the PHANGS-ALMA parent sample that (1) have inclinations $i \lesssim 70^\circ$, to minimize source blending and attenuation along the line-of-sight due to dust within the target, (2) avoid the Galactic plane ($|b| > 15^\circ$), to minimize the impact of Milky Way reddening and foreground stars, and (3) are sufficiently active ($\text{SFR} \gtrsim 0.3 M_\odot \text{ yr}^{-1}$), to ensure that wide-spread molecular cloud and star cluster populations are available for joint study. The resulting set of 38 galaxies chosen for HST observations is given in Table 1 along with basic properties relevant to their selection, which have been recently refined and updated (see A. K. Leroy et al. in preparation). VLT/MUSE optical integral field spectroscopy have been obtained for 19 of the PHANGS galaxies, and all of these are included by the HST selection criteria.

The sub-sample of 38 PHANGS-HST galaxies probes a full range of global properties covered by the PHANGS-ALMA parent sample, which is representative of the overall present-day spiral galaxy population. This is illustrated in Figure 1 (upper left panel), which shows M_* and SFR of the PHANGS sample and the subset tar-

³ After a recent update to the distance determinations, including the addition of new TRGB distances from our parallel ACS V and I band imaging (Section 3.2), we find that galaxies in the PHANGS-HST sample lie at distances between 4.4 and ~ 23 Mpc, with a median of ~ 16 Mpc (Figure 1). Uncertainties in distances that were used in the initial PHANGS galaxy selection, some of which were based on recession velocities corrected for peculiar motions based on a flow model, led to the inclusion of galaxies which lie beyond the initial ~ 17 Mpc limit. Further discussion of the impact of distance uncertainties on the PHANGS sample selection can be found in A. K. Leroy et al. (in preparation), while full details on the compilation of best available distances are provided in Anand et al. (2020), and summarized in Section 3.2.

⁴ Cycle 2 program 2013.1.00650.S (PI E. Schinnerer), Cycle 3 program 2013.1.01161.S (PI K. Sakamoto), Cycle 3 program 2015.1.00925.S (PI G. A. Blanc), Cycle 3 program 2015.1.00956.S (PI A. K. Leroy) and additional programs in Table 2, A. K. Leroy et al, in preparation.

² The original PHANGS-ALMA Large Program sample, from which PHANGS-HST targets were selected, consists of 74 galaxies. PHANGS has now extended the sample to 90 galaxies to include additional nearby galaxies with CO mapping available from the ALMA archive, as well as early-type galaxies, as explained in more detail in A. K. Leroy et al. (in preparation).

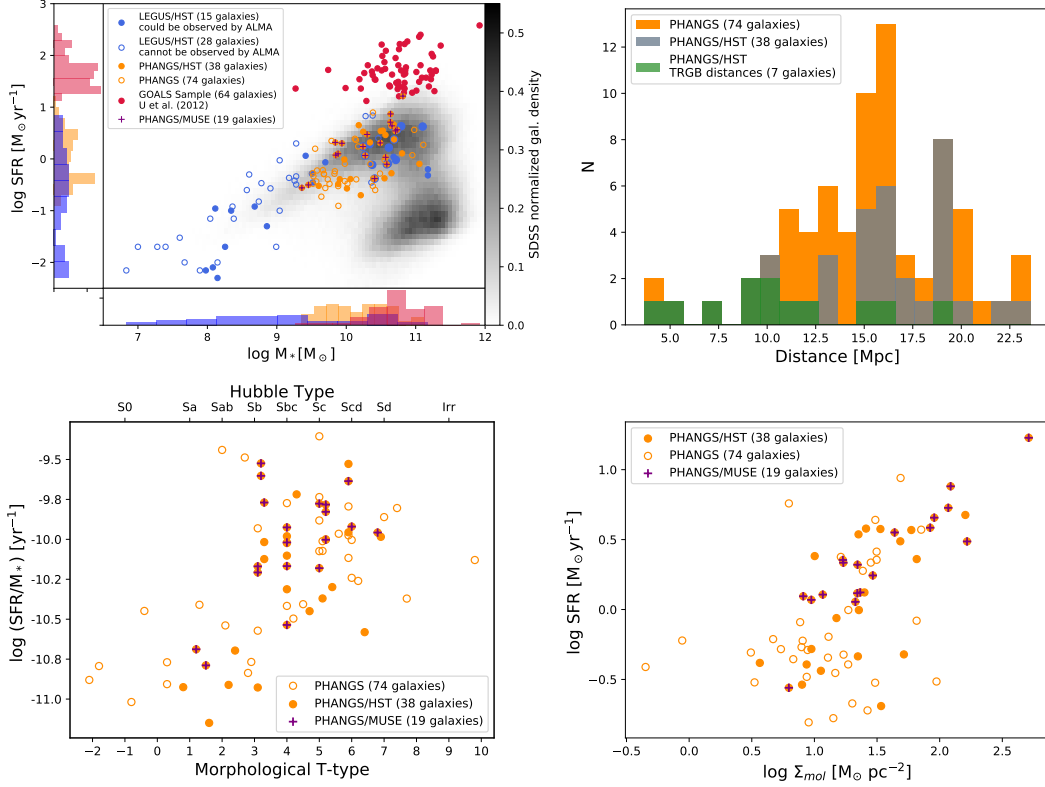


Figure 1. Upper left: Coverage of the SFR– M_* plane by galaxies in the parent PHANGS sample, and those targeted for HST observations. The PHANGS-HST sub-sample ($N = 38$) is representative of the $d \lesssim 20$ Mpc massive galaxy population on the local star-forming main sequence, which contain the bulk of molecular gas and present-day star formation (orange filled circles). Shown for context are: an SDSS local galaxy sample, which extends over a much larger volume to $z \lesssim 0.3$ (greyscale); the HST LEGUS sample (blue), which focuses on the nearest galaxies ($d \lesssim 11$ Mpc) and includes a significant number of lower mass dwarfs; and the GOALS sample (red), which targets luminous infrared galaxies. **Upper right:** Distribution of distances of galaxies in the PHANGS parent sample, and those selected for HST observations. Distances from updated compilation by Anand et al. (2020). The 7 new TRGB distances from Anand et al. (2020) based on PHANGS-HST parallel imaging with ACS are indicated (see Table 1). **Bottom panels:** PHANGS-HST also provides coverage of a full range of specific SFR, molecular gas surface densities, and spiral galaxy morphologies. Galaxies with MUSE IFU spectroscopy are indicated ($N = 19$).

geted with HST, overlaid on the locus occupied by star-forming galaxies from the Sloan Digital Sky Survey. Figure 1 shows that the PHANGS samples provide excellent coverage of the galaxy “main sequence” between stellar masses of $\sim 10^{9.5} - 10^{11} \text{ M}_\odot$. Main sequence galaxies in this stellar mass range are representative of the environments where the bulk of molecular gas and present-day star formation are found (Salim et al. 2007; Saintonge et al. 2017). The bottom panels of Figures 1 illustrate the coverage of specific SFR as a function of morphological type and the SFR as a function of the molecular gas surface density. The PHANGS-HST observations include spiral galaxies with morphological types of Sa through Sd, sSFRs from $\sim 10^{-10.5} - 10^{-9} \text{ yr}^{-1}$, SFR from $\sim 0.2 - 17 \text{ M}_\odot \text{ yr}^{-1}$, and Σ_{mol} from $\sim 10^{0.5} - 10^{2.7} \text{ M}_\odot \text{ pc}^{-2}$.

To place the PHANGS-HST survey in further context, nearby galaxies from two other major, comple-

mentary HST imaging programs are also shown in the upper left panel of Figure 1: HST LEGUS (Legacy ExtraGalactic Ultraviolet Survey; Calzetti et al. 2015), and GOALS (Great Observatories All-Sky LIRG Survey; Armus et al. 2009). As a Cycle 21 Treasury program, LEGUS also obtained 5-band UV-optical imaging to study star clusters in a representative sample of local galaxies (Adamo et al. 2017), but focused on the nearest systems ($\lesssim 11$ Mpc) to also enable the re-construction of star formation histories from individually resolved stars (Cignoni et al. 2018; Sacchi et al. 2018; Cignoni et al. 2019). LEGUS is therefore naturally dominated by lower mass dwarf and irregular galaxies, which comprise about half of its 50 galaxy sample (Cook et al. 2019). At the opposite extreme of the parameter space occupied by nearby star-forming galaxies, GOALS has obtained HST imaging in the B, I, and H filters for ~ 90 luminous infrared galaxies with thermal IR (8–1000 μm)

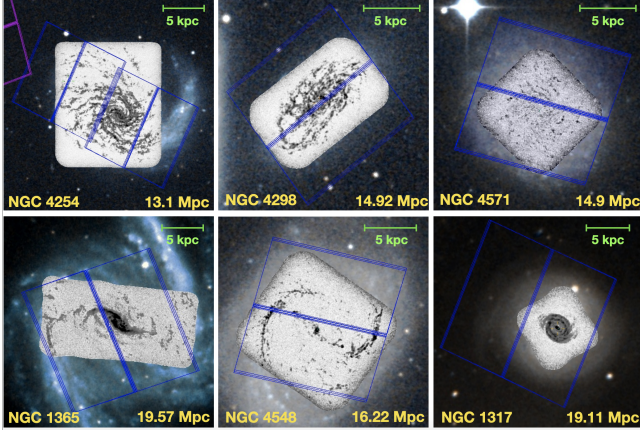


Figure 2. PHANGS-HST WFC3 UVIS footprints ($162'' \times 162''$) overlaid on PHANGS CO(2-1) ALMA maps for 6 galaxies in our sample of 38, showing the enormous diversity of molecular gas content and morphology in present-day massive star-forming galaxies. CO maps are overlaid on wider field DSS imaging. Scale bars and galaxy distance are shown in the upper and lower right corners respectively. **Top:** Targets showing decreasing molecular gas surface density and specific SFR, from left to right. **Bottom:** Impact of dynamical features on the gas distribution; two examples showing differing responses of the gas to the influence of a bar (left, middle) and an example of a ring feature (right). Our WFC3/UVIS observations are allowing us to find and characterize young stellar clusters and associations over the same area covered by these detailed CO maps, to create the first combined atlas of clouds and clusters across a representative sample of massive main sequence galaxies in the local universe.

dust emission greater than $10^{11} L_{\odot}$ (Haan et al. 2011; Kim et al. 2013). Such highly active star-forming galaxies are rare in the present-day universe, so the GOALS sample extends over much larger distances compared to LEGUS and PHANGS-HST. GOALS galaxies are located at distances of up to ~ 350 Mpc ($z < 0.088$), and hence studies of the stellar populations have focused on larger “clumps” (~ 90 pc, Larson et al. 2020). Currently PHANGS is the only program with uniform ALMA CO observations for a significant sample of nearby galaxies, but ultimately, analysis of all of these programs together are needed to fully understand the impact of galactic environment on star formation.

3. HST OBSERVATIONS

Imaging observations for the PHANGS-HST Treasury program (Cycle 26, PID 15654) began in April 2019 with an allocation of 122 orbits. Previous to this program, no HST wide-field UV imaging was available for 80% of the PHANGS-HST sample, and 60% also did not have any optical imaging with either WFC3 or ACS. Thus, PHANGS-HST provides a critical augmentation to the

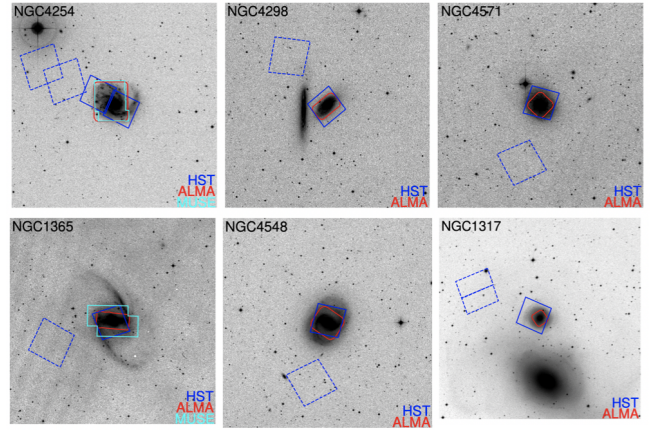


Figure 3. Figures showing the overlap of the PHANGS-HST WFC3 UVIS (blue), ALMA (red), and MUSE (where available; cyan) observation footprints, overlaid on DSS imaging for the same 6 galaxies as in Figure 2. A larger field ($20' \times 20'$) is shown relative to Figure 2 to illustrate the placement of the HST ACS parallel pointing (dashed lines). The WFC3 UVIS field-of-view is $162'' \times 162''$ and the ACS field-of-view is $202'' \times 202''$. Such footprint maps for the full PHANGS-HST sample can be found at <https://archive.stsci.edu/hlsp/phangs-hst/>.

HST archive for nearby spiral galaxies for which both star clusters and molecular clouds can be efficiently detected by HST and ALMA over galactic scales.

As discussed in Section 2, the PHANGS-HST sample contains a total of 38 galaxies. No new observations were conducted for 4 galaxies, since sufficient imaging for those targets were previously obtained by the LEGUS program.⁵ Altogether, new observations were planned for 43 fields in 34 galaxies. Observations for 40 fields were successfully completed by August 2020. Initial observations for 8 fields were corrupted due to guiding failures. Of these 5 have been successfully re-observed, and the remaining 3 fields⁶ have been re-scheduled for observation in Spring 2021.

To illustrate the PHANGS coverage of each galaxy, footprints of the HST and ALMA observations, together with those for VLT/MUSE when available, are provided at MAST at <https://archive.stsci.edu/hlsp/phangs-hst/>. Examples of these footprint overlays are given in Figures 2 and 3 for six galaxies chosen to span the range of molecular gas surface densities, specific SFRs, and dynamical features (rings and

⁵ NGC 0628, NGC 1433, NGC 1512, and NGC 1566. Another three galaxies in the PHANGS-HST sample also have observations available from LEGUS (NGC 3351, NGC 3627, NGC 6744), but additional observations were obtained to increase the coverage of the area of the disk mapped by ALMA in CO(2-1).

⁶ Both pointings for NGC 2903 and one pointing for NGC 5068.

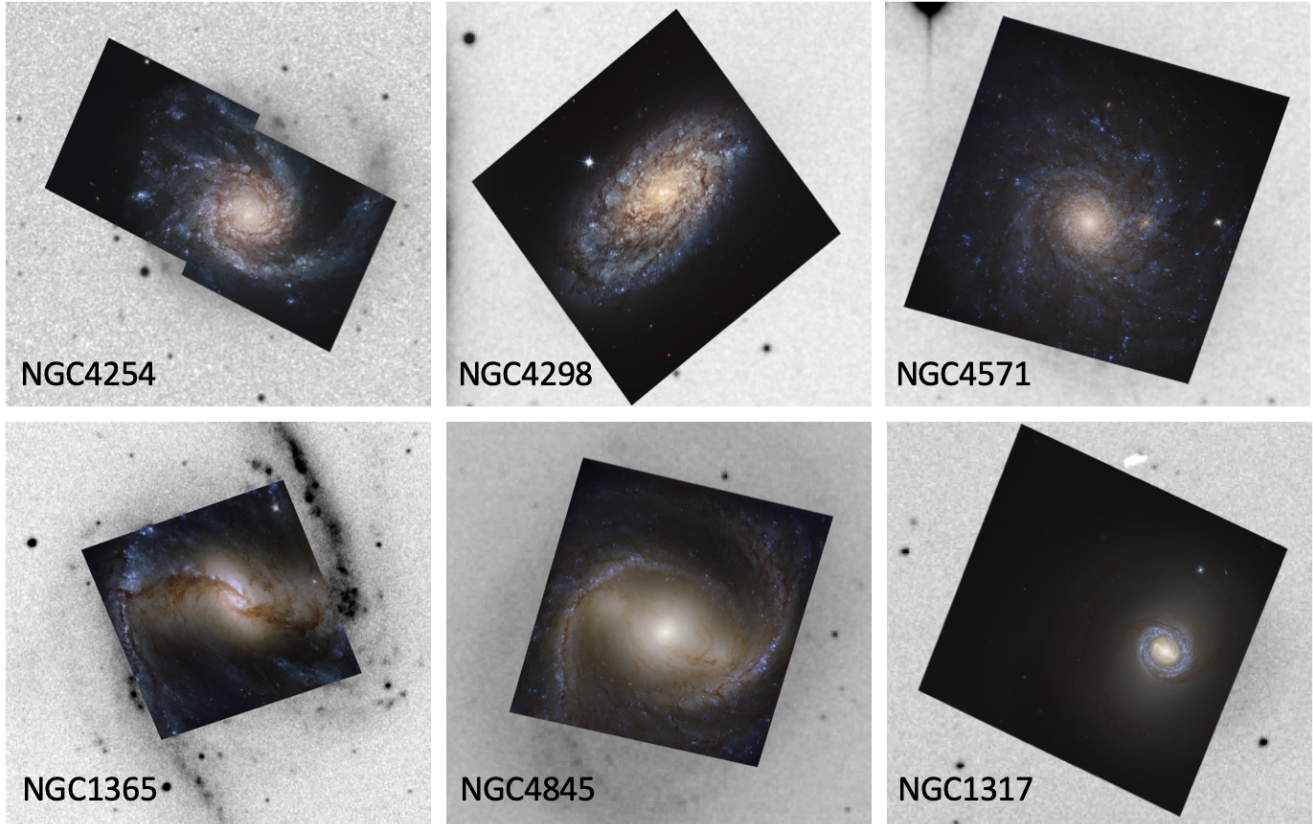


Figure 4. Color composites of PHANGS-HST imaging (Red: WFC3/UVIS F814W, Green: WFC3/UVIS F555W, Blue: WFC3/UVIS F438W+F336W+F275W), overlaid on DSS imaging for the same 6 galaxies as in Figures 2 and 3.

bars) present in the sample. Figure 2 focuses on the PHANGS-HST prime imaging area in the context of the PHANGS-ALMA CO(2–1) maps. Figure 3 shows a wider areal view of each galaxy with Digitized Sky Survey images,⁷ and overlays footprints of the PHANGS-HST prime+parallel, PHANGS-ALMA, and PHANGS-MUSE observations.

3.1. Prime Observations with WFC3

For each of the 43 new fields, we aim to cover the region mapped in CO(2–1) by ALMA in five filters: F275W (NUV), F336W (U), F438W (B), F555W (V), F814W (I). F275W is the shortest wavelength filter that avoids the 2175 Å dust feature, and in combination with the U and B bands serves to break the age-extinction degeneracy. The V and I bands are less affected by extinc-

tion and variation in the mass-to-light ratio, and serve to constrain the stellar mass.

For 31 fields (in 26 galaxies), new observations with the WFC3 UVIS camera were needed in all five filters. Three exposures with sub-pixel dithering were taken in each filter (the average pixel size of WFC3 UVIS is 0''.04), and all 15 exposures were obtained in a 3-orbit visit, yielding total exposure times of ~ 2200 s (NUV), ~ 1100 s (U), ~ 1100 s (B), ~ 670 s (V), ~ 830 s (I). A post flash of 5–10 e^- is applied for each exposure, with larger values in the shorter wavelength filters, to increase the background to 12 e^- , which is the recommended value to mitigate issues due to charge transfer efficiency (CTE) losses. The dither sequence is optimized to cover the WFC3 chip gap and to help recover the under-sampled point spread function (PSF).

For the other 12 pointings (in 8 galaxies), suitable WFC3 or ACS data in one or more of these filters were taken by prior programs. The available archival data were obtained from MAST and processed in a consistent manner with our new observations, and new imaging was obtained only for the missing filters within a 2-orbit visit.

⁷ The Digitized Sky Surveys were produced at the Space Telescope Science Institute under U.S. Government grant NAG W-2166. The images of these surveys are based on photographic data obtained using the Oschin Schmidt Telescope on Palomar Mountain and the UK Schmidt Telescope. The plates were processed into the present compressed digital form with the permission of these institutions.

3.2. Parallel Observations with ACS

While the primary observational goal of the PHANGS-HST survey is to obtain UV-optical imaging of the star-forming disk, we also simultaneously observe the galaxy halo with the Advanced Camera for Surveys Wide Field Channel (ACS/WFC) in “parallel” mode. Such parallel observations can potentially yield measurements of the galaxy distance if the tip of the red giant branch (TRGB) can be identified in a color-magnitude diagram of halo stars. Thus, we have designed our observations so that ACS imaging in F606W and F814W, filters commonly used for TRGB analysis (e.g., [McQuinn et al. 2017](#); [Anand et al. 2018](#)) accompanies each WFC3 “prime” observation.

For the range of distances and angular sizes of the PHANGS-HST galaxies, the ACS field-of-view generally falls on the halo of the target galaxy when WFC3 is centered on the galaxy itself (Figure 3). Given that the science requirements of PHANGS-HST constrain the positioning of the prime pointings, optimizing placement of the parallel fields (as in a focused TRGB program) is a secondary priority and is restricted by the fixed spatial offset of the two cameras on the focal plane. For galaxies with relatively large angular sizes, the parallel observations may include portions of the outer disk. For smaller galaxies, the parallels may be too far to capture a significant number of halo stars. To the extent possible, ORIENT constraints were imposed to prevent the ACS field from entirely falling on the galaxy disk, on nearby galaxy neighbours, and/or on extremely bright foreground stars. For some targets with large angular sizes where it was not possible to avoid the disk completely, the field was positioned along the major axis to help differentiate between disk and halo stars. In several cases, the desired ORIENT constraints were lifted or relaxed to allow guide stars to fall into the area of the focal plane accessible to the Fine Guidance Sensors.

The five-band prime observations with WFC3/UVIS were sequenced in each orbit to optimize exposure time in the parallel observations without impacting the primary observations. As discussed in the previous section, WFC3 observations for each pointing required 2 or 3 orbits, depending on whether suitable HST archival observations of the galaxy disk were already available. For 2-orbit visit pointings, the total exposure times in the ACS parallel V and I images are ~ 2100 s each, while for the 3-orbit visits they are about ~ 3500 s and 3200 s, respectively. In both cases, three exposures were taken in each filter.

Distance constraints resulting from analysis of the TRGB based upon parallel imaging obtained in the first year of the PHANGS-HST program (for 30 galaxies

through 2020 July) are presented in [Anand et al. \(2020\)](#). There, we report TRGB distances for 10 PHANGS galaxies, 4 of which are the first published TRGB distance measurements for those galaxies (IC 5332, NGC 2835, NGC 4298, NGC 4321) and 7 of which represent the best available distances (IC 5332, NGC 2835, NGC 3621, NGC 4298, NGC 4826, NGC 5068, NGC 6744). The latter are highlighted in the distance distribution in Figure 1 (top right panel), with distances listed in Table 1. Results from the remaining seven parallel fields (in six galaxies: IC 1954, NGC 0685, NGC 1097, NGC 2903-N/S, NGC 5068⁸, NGC 7496) will be published after the completion of the PHANGS-HST observations, which is, again, anticipated by mid-2021.

4. DATA PROCESSING PIPELINE

To enable the joint HST-ALMA study of star formation in basic units of star clusters, associations, and molecular clouds, we have developed an extensive HST data processing pipeline which produces inventories of stars (point sources), compact star clusters, and stellar associations across multiple physical scales in each galaxy. The pipeline yields aligned, mosaicked images in all five filters as well as catalogs of observed (e.g. photometry and morphological parameters) and physical properties (stellar masses, ages, reddenings, derived through SED fitting). Ultimately, the PHANGS-HST star cluster and association catalogs will be cross-correlated with the PHANGS-ALMA molecular cloud catalogs (E. Rosolowsky et al. submitted; A. Hughes et al. in preparation) and PHANGS-MUSE HII region catalogs (F. Santoro et al. in preparation). Python packages and high level science products from this pipeline will be publicly released and are described in Section 5.

Here, we summarize the overall strategy of the pipeline and provide a framework for subsequent papers which document each of the major components in detail. The key steps in the PHANGS-HST pipeline are:

1. Image drizzling, mosaicking, astrometric calibration (this paper; Section 4.1)
2. Source detection (D. Thilker et al. in preparation; Section 4.2)
3. Identification of bright, isolated star clusters for determining aperture corrections (S. Deger et al. in preparation; Section 4.3)

⁸ Re-observation for guiding failure. WFC3 prime observations were corrupted, but most parallel observations for this target were still usable.

4. Derivation of aperture corrections for star clusters (S. Deger et al. in preparation; Section 4.3)
5. Aperture photometry (D. Thilker et al. in preparation; S. Deger et al. in preparation; Section 4.4)
6. Selection of candidate star clusters (D. Thilker et al. in preparation; Section 4.4)
7. Morphological classification of candidate star clusters (Wei et al. 2020, B. Whitmore et al. in preparation; Section 4.5)
8. SED fitting of star cluster photometry (Turner et al. 2021); Section 4.6)
9. Identification, photometry, and SED fitting of stellar associations (K. Larson et al. in preparation; Section 4.7)

Our processing workflow reflects common practice for the production of catalogs of compact star clusters in nearby galaxies (Adamo et al. 2017), with the following key augmentations. First, selection criteria are based on measurement of a series of concentration indices (CI; the difference in photometry measured with circular apertures of two different radii) rather than a single concentration index (Section 4.4). Second, we inject model star clusters into the HST imaging to aid the definition of selection criteria to separate candidate clusters from point sources and other interlopers and build a foundation to estimate completeness in future work (Section 4.4). Third, we utilize convolutional neural network models, as discussed in Wei et al. (2020), to supplement human visual inspection, with the goal of eventually automating morphological classification of candidate star clusters, as this has been a limiting step in past cluster studies (e.g. Adamo et al. 2017, B. Whitmore et al. in preparation). Fourth, we separate the process for selecting multi-peaked stellar associations from single-peaked compact stellar clusters, by applying a watershed algorithm to point sources to identify associations at physical scales from 8 pc to 64 pc (Section 4.7). This produces a far more complete inventory of young stellar populations, which is crucial for robust comparisons with molecular clouds.

A flowchart illustrating the steps in the pipeline as summarized below is provided in Figure 5.

4.1. Drizzling, Mosaicking, Astrometric Calibration

The process used to drizzle and mosaic the HST imaging data follows current standard procedures.

Data acquired for PHANGS-HST are first obtained from MAST, along with other suitable archival data

taken by previous programs. These “FLT” exposures have been processed through the standard Pyraf/STSDAS CALACS or CALWFC3 software in the archive, which performs initial data quality flagging, bias subtraction, gain correction, bias stripe removal, correction for CTE losses, dark current subtraction, flat-fielding and photometric calibration, resulting in “FLC” FITS files for each ACS/WFC and WFC3/UVIS exposure.

The PHANGS-HST pipeline is based on the STScI-supported software package DRIZZLEPAC to combine exposures and improve sampling of the PSF, and is used for the prime observations targeting the galaxy disk in a two step drizzle procedure. The parallel observations are treated separately as discussed in Anand et al. (2020).

The pipeline takes the FLC FITS files retrieved from MAST as input to produce combined images for each filter, which are all aligned and drizzled onto a common grid with pixel scale of $0''.04$ (the native WFC3 pixel scale), with astrometry calibrated with GAIA DR2 sources (Gaia Collaboration et al. 2018; Lindegren et al. 2018). The latter is essential for proper alignment of the HST imaging with ALMA and VLT/MUSE data and for joint study of the three datasets.

The V-band imaging (WFC3 F555W) is used as the reference for positioning of the images in all other filters (NUV, U, B, I) and to define the common pixel grid. Using the F555W FLC files from MAST for each pointing, the sky positions of the centers and corners of the images are calculated to define a search area to query the ESA DR2 GAIA catalogue. The TWEAKREG routine then matches the GAIA sources to the objects detected in the F555W drizzled image and calculates average shifts (with accuracy typically better than 0.1 pixel) to correct the astrometric solution. The number of GAIA sources found in a given F555W HST pointing varies from as few as 15 sources to a maximum of 317 with an average of 40 sources. The TWEAKBACK routine is then used to propagate the corrected WCS solution back to the original F555W FLC images. Finally, TWEAKREG and TWEAKBACK are used again, but now with the drizzled images for the other four filters to find sources in common with those detected in F555W, and to align to the F555W image.

The final drizzle combination is carried out with sky subtraction using the “globalmin+match” method for sky calculation. ASTRODRIZZLE first finds a minimum “global” sky value for each chip/image extension in all input images and then uses the “match” method to compute differences in sky values between images in common sky regions and to equalize the sky values between images. The final DRC FITS files are in units of

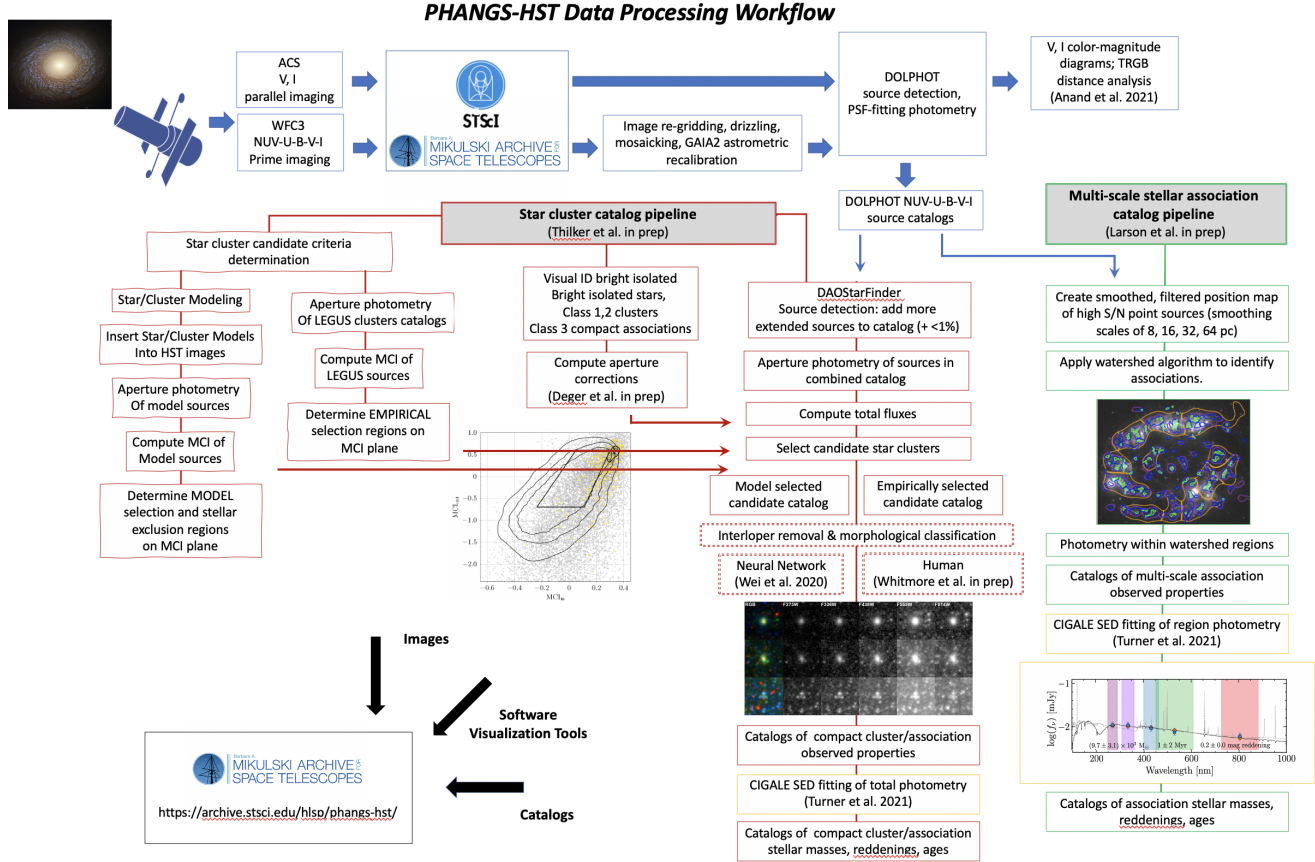


Figure 5. Flowchart illustrating the overall steps in the PHANGS-HST star cluster and multi-scale stellar association catalog pipeline. Chart begins at the upper-left corner with the acquisition of HST imaging, proceeds along the top, and the flows along parallel branches from top to bottom.

$e^- s^{-1}$ and are registered with North up and East left as usual. “EXP” (exposure time) and “ERR” (error) weight (WHT) maps, calculated from the contribution of all input exposures to a given output pixel, are also produced. The ERR maps includes all noise sources from detector and sky and are used to compute uncertainties in photometry downstream in the pipeline.

Color composites of the drizzled, mosaicked HST imaging are shown in Figure 4 for the same six galaxies featured in Figures 2 and 3.

4.2. Source Detection and Photometry

The principal method of source detection in the PHANGS-HST pipeline is provided by the DOLPHOT photometry package (v2.0 Dolphin 2002), which is based on PSF-fitting and operates on the FLC files to detect and deblend sources in HST imaging. The DOLPHOT source catalogs provide a common starting point for identification of both multi-peaked stellar associations and single-peaked compact star clusters. The drizzled V-band image is used as the positional reference and sources are

detected to 3.5σ with PSF-fitting performed at the same image positions in all bands.

Compact star clusters have effective radii between 0.5 pc to about 10 pc (Portegies Zwart et al. 2010; Ryon et al. 2017). At the distances of the galaxies in the PHANGS-HST sample, such objects will have angular sizes close to the HST WFC3 resolution (i.e., 2 pixels $\sim 0''.08$; from 1.7 to 9 pc for the distances of the galaxies in the sample) and will appear sufficiently point-like to be captured by DOLPHOT. To ensure that the catalogs include star clusters with light profiles which may be more extended than the sources detected by DOLPHOT, source detection is also performed with the python implementation of DAOPHOT, DAOSTarFinder (within the photutils astropy-affiliated package), with a kernel FWHM of 2.5 pixels. The merged DOLPHOT and DAOSTarFinder catalogs provide the source lists from which compact star cluster candidates are identified, while the branch of the pipeline which identifies multi-peaked stellar associations (Section 4.7) relies only upon the DOLPHOT catalogs.

Following source detection, the star cluster pipeline then uses the positions from the merged DOLPHOT-DAOStarFinder catalog to perform aperture photometry in all five filters. Photometry is measured in circular apertures with a 4 pixel radius, with background determined in an annulus between 7–8 pixels around the aperture. An aperture correction (Section 4.3) is applied which yields the total fluxes for sources ultimately identified as compact star clusters. Photometry is also measured in a series of other circular apertures (with radii from 1–5 pixels) to measure concentration indices to distinguish star cluster candidates from stars and other sources/artifacts (Section 4.4). Catalogs with these measurements are produced for each galaxy, and on average contain about $\sim 500,000$ sources, with detections from DAOStarFinder contributing less than $\sim 1\%$ of objects with V-band $S/N > 10$.

D. Thilker et al. (in preparation) discuss in detail the parameter choices for both DOLPHOT and DAOStarFinder and pipeline procedures for obtaining aperture photometry and computing errors.

4.3. Star Cluster Aperture Corrections

Star clusters, in particular those that are young, can be found in crowded regions. Direct, accurate measurement of the total flux is often not possible since the outer light profile is frequently contaminated by other sources. Thus, HST photometry of compact star clusters in galaxies beyond the Local Group is typically measured with a tight aperture that captures $\sim 50\%$ of the total flux, and then a correction, determined from bright, isolated clusters, is applied (Adamo et al. 2017; Cook et al. 2019).

S. Deger et al. (in preparation) present a detailed discussion of procedures used to determine average aperture corrections for each field and their uncertainties. In summary, the V-band images are visually inspected to identify a few dozen well-detected, isolated, compact clusters, and these objects are used to compute an average correction for each field. Fixed offsets, based on the change in the WFC3 PSF with wavelength (which has a minimum FWHM of $0''.067$ in the V band, and increases to $\sim 0''.075$ in the NUV and I bands) are used to calculate the corresponding corrections for photometry in the NUV, U, B, and I bands, since direct measurements from growth curves in those filters for bright sources in the V-band which are very red or blue can be noisy (Cook et al. 2019, S. Deger et al. in preparation). By construction, the resulting V-band corrections are ~ 0.75 mag. The corrections are larger by 0.19, 0.12, 0.03 and 0.12 mag for the NUV, U, B, and I band, respectively.

4.4. Star Cluster Candidate Selection

The PHANGS-HST pipeline identifies cluster candidates based on their V-band photometric and morphological properties. In previous work, the concentration index (computed as the difference between photometry measured in circular apertures with radii of 1 and 3 pixels; CI_{13} or simply CI) has been generally used to remove sources likely to be stars from consideration (e.g. Adamo et al. 2017; Cook et al. 2019). To determine the threshold to separate stars from cluster candidates, CIs have been measured for samples of a few dozen objects in each image which are visually identified and verified to be isolated, bright point sources. These measurements are then compared with the CI distribution for an analogous sample of compact star clusters (which are also used to derive aperture corrections).

For PHANGS-HST, D. Thilker et al. (in preparation) build upon this method to develop candidate selection criteria based on multiple concentration indices (MCI), rather than a single concentration index. We measure fluxes in circular apertures with radii of 1.0, 1.5, 2.0, 2.5, 3.0, 4.0, and 5.0 pixels, and we define two metrics to characterize the light profiles between 1–2.5 pixels (MCI_{in}) and 2.5–5 pixels (MCI_{out}), where

$$MCI \equiv \frac{1}{3}(NCI_{ab} + NCI_{bc} + NCI_{cd}), \quad (1)$$

where a, b, c, d represent the radii of the apertures, and

$$NCI_{ij} \equiv 1 - \frac{CI_{ij}}{CI_{ij, \text{fiducial}}} \quad (2)$$

is a CI normalized by $CI_{ij, \text{fiducial}}$, defined to be the CI of a Moffat profile (Moffat 1969) with a FWHM of 2 pixels and a power law of 3 for the extended halo, which represents a relatively compact cluster. The choice of normalization is arbitrary, and enables the various CI to be meaningfully averaged. With these definitions, clusters measured on HST optical images generally have values of $-0.5 \lesssim MCI_{in} \lesssim 0.2$, $-2 \lesssim MCI_{out} \lesssim 0.6$ (see Figures 6 and 7). MCI_{in} is anti-correlated with the standard CI_{13} , as would be expected from their definitions, with more compact sources characterized by larger MCI values (i.e. more concentrated), which is the opposite of the sense of the standard CI_{13} . By construction, the fiducial cluster lies at the origin of the MCI_{in} – MCI_{out} plane.

Selection regions are then defined in two ways on the MCI_{in} – MCI_{out} plane to generate two types of candidate lists based on: (i) the locus of star clusters identified by the HST LEGUS program (Figure 6), and (ii) the loci of synthetic star clusters inserted into the V-band imaging (Figure 7). That is:

1. Empirical selection criteria in the MCI plane are defined using catalogs of visually inspected clus-

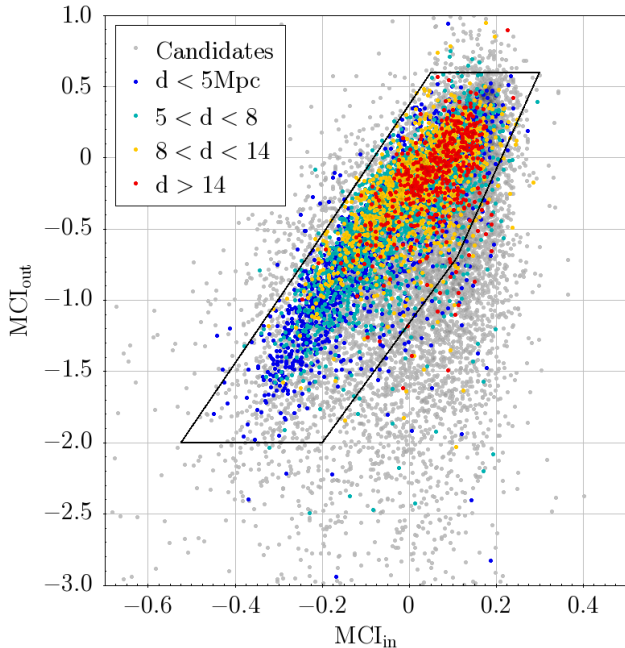


Figure 6. Empirically defined selection region for compact star cluster candidates in the multiple concentration index (MCI; see Equation 1) plane. The selection region is based on visually verified class 1 and 2 clusters from 30 galaxies studied by the LEGUS program (Calzetti et al. 2015; Adamo et al. 2017, colored points; <https://archive.stsci.edu/prepds/legus/dataproducts-public.html>). The larger set of candidates from LEGUS are also shown (grey points). Clusters are color-coded based on the distance of their host galaxy. The lower bound of MCI_{out} increases as the distance of the host galaxy increases (see also Figure 7), since the physical resolution decreases and clusters appear more compact.

ters published by the HST LEGUS program for 34 HST fields in 30 galaxies⁹. D. Thilker et al. (in preparation) measure the MCI values for the LEGUS compact star clusters and associations from the LEGUS HST V-band imaging. The adopted selection regions are shown together with the positions of the LEGUS cluster candidates and visually verified clusters in Figure 6. The lower bound of MCI_{out} increases as the distance of the host galaxies increases since clusters will be less resolved and appear more compact at larger distances. Initial analysis with PHANGS-HST visually-inspected clusters suggests that the density of clusters does rapidly drop beyond the boundaries of this region, but a more careful investigation of such completeness issues will be the

⁹ <https://archive.stsci.edu/prepds/legus/dataproducts-public.html>

subject of continuing work, as discussed further below.

2. Selection criteria in the MCI plane are also defined based on model star clusters. Synthetic clusters are generated with Moffat profiles, which again are parameterized by the effective radius (in units of the FWHM) and the power law of the extended halo (η). The modeling includes 216 distinct Moffat profiles, spanning $0.5 \text{ pix} \leq \text{FWHM} \leq 7 \text{ pix}$ and $0.75 \leq \eta \leq 4$. Models are generated for each of these profile types with a distribution of ~ 4000 apparent magnitudes. The magnitudes are computed from the distance of the galaxy and V-band luminosities based on solar-metallicity, single-aged stellar population models of Bruzual & Charlot (2003), for a grid of masses ($10^3 - 10^5 M_{\odot}$), ages (1-1000 Myr), and extinctions ($0 \leq A_V \leq 0.5 \text{ mag}$). The synthetic clusters are randomly inserted into the V-band images 200 at a time, and aperture photometry is performed with the same procedure used to measure real sources. In total, $\sim 4 \times 10^6$ clusters are inserted. The MCI values from these synthetic clusters are plotted on the $MCI_{\text{in}} - MCI_{\text{out}}$ plane to form a 2D histogram with a bin size of 0.01, and a contour enclosing the locus is derived. Contours are also derived for MCI bin sizes of 0.02 and 0.04, resulting in three different selection regions of increasing size for each field.

For both selection methods, the regions in the MCI plane dominated by stars (point sources) as detected by DOLPHOT, are defined for each field and used to exclude objects. Figure 7 shows both the synthetic and empirical cluster selection regions for four galaxies at a range of distances together with the stellar exclusion region.

In addition to having MCI values that are within one of the selection regions but outside of the stellar region, candidate star clusters must also satisfy basic criteria: V-band photometry measured in a 4 pixel radius must have $S/N \geq 10$, and the source must also be detected in at least two other bands with photometric error $\leq 0.3 \text{ mag}$. The faintest sources in the resulting candidate lists for fields with the standard V-band exposure time of 670 s have total V-band magnitudes of ~ 24.6 , which corresponds to absolute magnitudes between -4.2 and -7.8 for the distance range spanned by the PHANGS-HST galaxies.

Finally, all sources with total, absolute V-band magnitudes (i.e. after applying aperture correction) brighter than -10 mag , and MCI values that are plausible for clusters or stars ($-0.55 \leq MCI \leq 0.45$) are kept as candidates, as they are unlikely to be single stars given

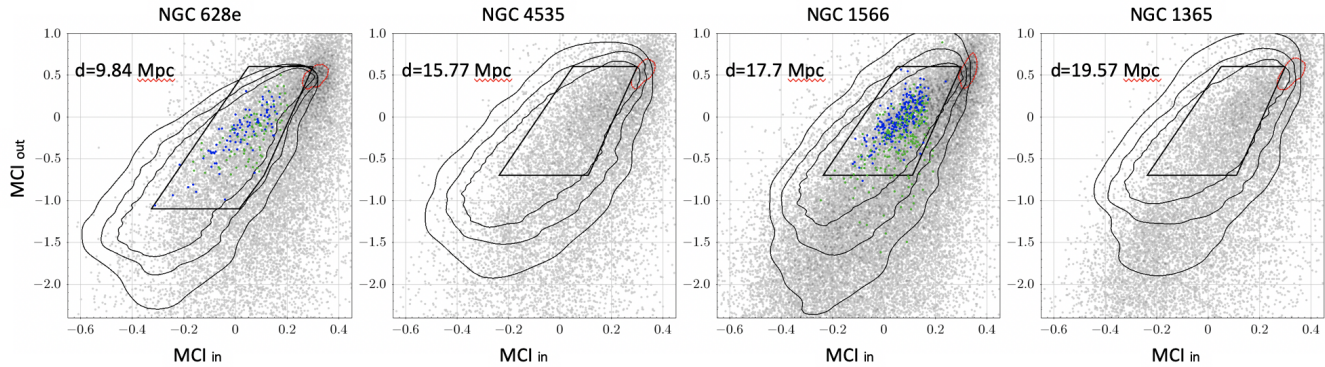


Figure 7. MCI selection regions defined using synthetic star clusters (large contours) for four galaxies (NGC 0628 east pointing, NGC 4535, NGC 1566, NGC 1365) at increasing distances from left to right. The empirical selection regions (polygon, same as in Figure 6) are shown for comparison. Cluster candidates are selected from source lists of potential candidates which satisfy basic signal-to-noise criteria (grey), excluding sources in the stellar (point source dominated) region (small red contour). Candidates within the empirical selection region are visually inspected and classified to a V-band magnitude limit of ~ 24 mag. The classification of the larger samples of candidates identified with the synthetic cluster MCI selection regions will be automated using convolutional neural network models. Sources outside the empirical and synthetic cluster selection regions are retained as candidate clusters if they exceed the Humphreys-Davidson luminosity limit for stars. NGC 628 and NGC 1566 are also in the LEGUS sample, and previously published, visually verified class 1 (blue) and class 2 (green) clusters, are also shown for those galaxies.

the Humphreys-Davidson limit (the observed maximum luminosity of stars in the LMC, thought to be due to a modified Eddington Limit; Humphreys & Davidson 1979; Lamers & Levesque 2017).

The number of candidates identified using the empirical MCI selection regions varies from many hundred to several thousand sources for each field, with a median of ~ 1000 (Figure 8), and should ultimately yield samples of compact star clusters similar to those studied in previous work. The variation in candidate sample sizes reflects the variation in global sSFRs for the PHANGS-HST galaxies which span a factor of ~ 10 (Figure 1). The synthetic cluster MCI selection casts a wider net for potential clusters (Figure 7), and yields candidate samples about a factor two larger than the empirical selection (Figure 8). These larger samples enable analysis of potential incompleteness in previous star cluster studies, in particular for more diffuse clusters which appear to be rare.

These new selection methods, based on the measurement of multiple CI and the use of model star clusters, provides a solid foundation for quantitative investigation of structural properties including: which model clusters actually exist in nature, whether certain clusters are likely to be bound or unbound, and how their morphologies evolve with time. The methodology will also facilitate characterization of cluster completeness levels (e.g. Johnson et al. 2015) in the future. D. Thilker et al. (in preparation) discuss in more detail the utility of this approach to cluster selection.

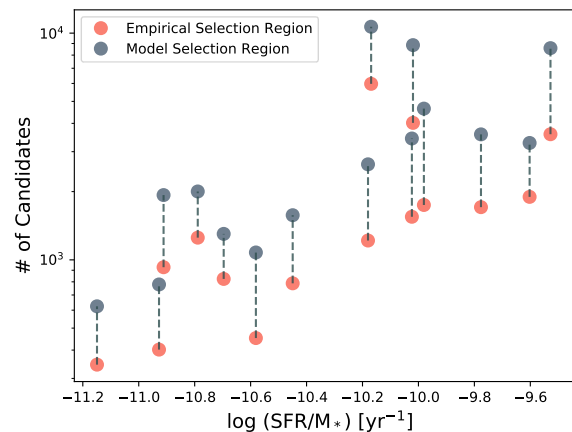


Figure 8. The number of compact star cluster candidates found in the first 15 galaxies processed through the PHANGS-HST pipeline, shown as a function of the sSFR. Candidates identified using the empirical selection regions are shown in red, while those resulting from the larger selection regions based on synthetic clusters are shown in grey. These cluster candidates undergo a process of inspection to further remove contaminants and sort the objects into three morphological categories using a combination of human visual classification and automated classification by convolutional neural network models as summarized in Section 4.5, and described in detail in Wei et al. (2020), and B. Whitmore et al. (in preparation).

4.5. Star Cluster Candidate Inspection and Morphological Classification

The candidate star clusters then undergo a process of inspection to further remove contaminants and to sort the clusters into different morphological categories. A combination of human visual inspection and automated inspection with convolutional neural network models is performed as follows:

- Candidates identified with the empirical MCI selection region are visually inspected by co-author BCW. Objects with total V-band magnitude to a limit of ~ 24 mag receive visual classifications.
- The larger samples of candidates identified with the synthetic cluster MCI selection regions are classified by convolutional neural network models, as described below. Candidates identified using the empirical selection region generally lie within the largest synthetic cluster selection area (Figure 7), and hence will have both neural network and human visual classifications.
- Human visual inspection of fainter candidates and those beyond the boundaries of the empirical selection region are performed on an ad-hoc basis to evaluate and monitor the performance of the neural network models.

For PHANGS-HST, we adopt the general classification scheme used by LEGUS as described in Adamo et al. (2017) and Cook et al. (2019):

- Class 1: compact star cluster – single peak, circularly symmetric, but radial profile more extended relative to point source
- Class 2: compact star cluster – similar to Class 1, but elongated or asymmetric
- Class 3: compact stellar association – asymmetric, multiple peaks
- Class 4: not a compact star cluster or compact stellar association (e.g. image artifacts, background galaxies, individual stars or pairs of stars)

Examples of Class 1, 2, 3 objects are shown in Figure 9. B. Whitmore et al. (in preparation) provide a detailed description of the process of visual inspection and morphological classification, and discuss differences in the application of this scheme for Class 3 objects relative to the LEGUS project (i.e. we require evidence of 4 or more peaks within a radius of 5 pixels in PHANGS-HST). A brief history of star cluster classification is also given there (also see Wei et al. 2020, Section 2). While we continue to include Class 3 objects in our compact

cluster catalogs, we note that this is mainly for historical continuity with the LEGUS project. This detection method is optimized for single-peaked compact clusters, and leads to a high-level of incompleteness for multi-peaked stellar associations. Instead, we introduce a new identification process for stellar associations, based on a watershed algorithm, which provides a far more complete inventory of the star formation hierarchy at multiple physical scales, as will be discussed in Section 4.7 and K. Larson et al. (in preparation).

It should be noted that it is debated whether individual classifications distinguish between gravitationally bound clusters and unbound associations, which may form and evolve under distinct conditions (Gieles & Portegies Zwart 2011; Kruijssen 2012; Krumholz et al. 2019; Ward et al. 2020). On average however, Class 1 should contain the highest percentage of bound clusters, and Class 3 should have the highest percentage of unbound associations (see B. Whitmore et al. in preparation for further details).

When observations and reductions are completed in 2021, PHANGS-HST will generate up to $\sim 80,000$ star cluster candidates for inspection and classification. In previous large studies of star clusters, the process of visual inspection has been a limiting step, which motivated the investigation of automated machine learning techniques (Messa et al. 2018; Grasha et al. 2019; Perez et al. 2020). In Wei et al. (2020), we studied the application of deep transfer learning techniques to train convolutional neural network (CNN) to classify star cluster candidates according to the scheme above. Deep transfer learning involves the tuning of a pre-trained network, for example, based on the ImageNet library of everyday objects¹⁰. In principle, this approach enables CNNs to be successfully trained with small samples (i.e. hundreds to a thousand images), which is the current size of HST star cluster samples with visual classifications. It provides an alternative to the process of training all network layers from scratch which requires samples which are an order of magnitude larger. The results of Wei et al. (2020) were encouraging, as the prediction accuracies (70%, 40%, 40–50%, 50–70% for Class 1, 2, 3 star clusters, and Class 4 non-clusters, respectively) were found to be competitive with the consistency between different human classifiers. The neural network models presented in Wei et al. (2020) provide a starting point for automated classification of the PHANGS-HST and other HST star cluster candidate samples, which can continue to be optimized. B. Whitmore et al. (in preparation)

¹⁰ <http://www.image-net.org/>

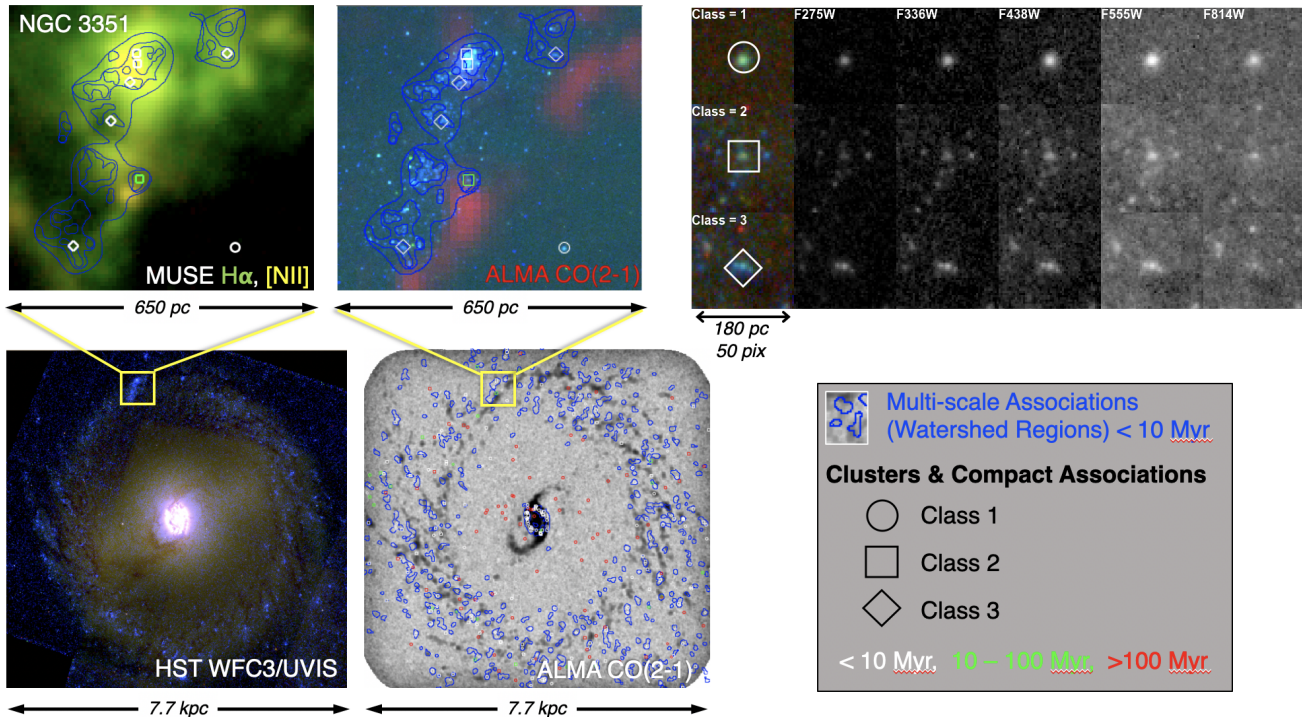


Figure 9. Structures across the physical scales of the star formation hierarchy in NGC 3351, identified by the PHANGS-HST pipeline, from single-peaked compact star clusters, the densest structures, to larger scale multi-peaked stellar associations. **Bottom left:** Color composite of WFC3/UVIS F275W+F336W (blue), WFC3/UVIS F435W+F555W (green), WFC3/UVIS F814W (red). **Bottom right:** Young stellar associations (<10 Myr) traced by the watershed-based method of K. Larson et al. (in preparation, blue contours), together with all compact clusters and associations with human visual classifications (Class 1: circles, Class 2: squares, Class 3: diamonds; color coded by age as indicated), overlaid on the PHANGS-ALMA CO(2-1) map. A 650 pc section of the outer ring (yellow box) is shown in more detail in the top left and middle panels. All three classes of compact clusters and associations are represented in the selected section, and the magnified view allows all four levels traced by the watershed method (64 pc, 32 pc, 16 pc, 8 pc) to be clearly shown. **Top left:** Magnified view using an H α map constructed from the VLT/MUSE IFU data cube. **Top middle:** Magnified view using a color composite image where CO is now shown in red. **Top right:** Further magnification of 180 pc areas centered on examples of the three classes of compact clusters and associations found in the selected 650 pc section of the outer ring in all PHANGS-HST filters.

present results of the current Wei et al. (2020) models applied to clusters candidates in five PHANGS-HST galaxies. The analysis includes detailed comparison between visual and automated classifications, from overall prediction accuracy to differences in ages, UBVI color-color diagrams, and stellar mass functions, as well as discussion of additional work to improve performance.

4.6. SED Fitting

To derive ages, masses, and reddenings for the sources classified as star clusters and associations, we use a modified version of CIGALE¹¹ (*Code Investigating GALaxy Emission*; Burgarella et al. 2005; Noll et al. 2009; Boquien et al. 2019), a publicly available SED fitting package developed for galaxies. Our modifications, which

support the fitting of single-age populations and provide modeling options to facilitate comparison to prior SED modeling results for star clusters, are available in dedicated branches, SSP and SSPmag respectively, of the public git repository¹² of CIGALE. Turner et al. (2021) reports on these modifications and the analyses performed to validate the code.

SED fitting with CIGALE is performed on the 5-band photometry (NUV-U-B-V-I) for both compact star clusters, and stellar associations. The fitting is based on the simple (single-aged) population synthesis models of Bruzual & Charlot (2003), assuming solar metallicity and a Chabrier (2003) IMF (with standard mass limits of 0.1–100 M_{\odot}), and no addition of nebular emis-

¹¹ <https://cigale.lam.fr>

¹² <https://gitlab.lam.fr/cigale/cigale.git>

sion. The Cardelli et al. (1989) extinction curve with $R_V = 3.1$ is used and a maximum $E(B-V) = 1.5$ mag is imposed. The reasoning for these choices is also discussed in Turner et al. (2021).

Adopting the same assumptions and theoretical models as used in LEGUS, Turner et al. (2020) find very similar cluster ages and masses. Quantitatively, fits to identical cluster datasets yield (logarithmic) medians in the ratios of ages and masses for the two surveys of 0.001 ± 0.017 dex and 0.003 ± 0.011 dex, respectively.

4.7. Stellar Association Identification

The majority of star formation occurs in stellar associations (Lada & Lada 2003; Ward & Kruijssen 2018; Ward et al. 2020; Wright 2020, and references therein). Compact star clusters, the focus of the previous sections, are formed only in the densest peaks of the star-formation hierarchy (Elmegreen 2008; Kruijssen 2012) and contain between 1~50% of the total star formation in galaxies (Kruijssen 2012; Adamo et al. 2015; Johnson et al. 2016; Chandar et al. 2017; Krumholz et al. 2019; Adamo et al. 2020). To produce catalogs of stellar associations, methods distinct from those used to identify single-peaked compact clusters are needed to segment the light distribution over larger physical scales and to probe further into the star-formation hierarchy. Development of such methods are particularly important for obtaining complete inventories of the youngest stellar populations ($\lesssim 10$ Myr) and are a critical component of joint analysis with molecular clouds.

For PHANGS-HST, K. Larson et al. (in preparation) develop a technique to produce catalogs of stellar associations spanning scales from 8 to 64 pc. The technique builds upon the watershed routine in the scikit-image python package (SKIMAGE.SEGMENTATION.WATERSHED van der Walt et al. 2014), which is based on the concept of geological watersheds. The routine identifies regions by “flooding” an image, given a set of markers as the starting points. In addition to the image requiring segmentation, the inputs needed by WATERSHED are a list of marker positions, and an image mask which defines the areas over which regions are allowed to grow.

K. Larson et al.’s technique deploys WATERSHED on a smoothed, filtered map of the positions of point sources (rather than directly on the HST images), and uses a two parameter procedure to determine the marker positions and produce the image mask from these position maps. The smoothed, filtered, positional maps are produced as follows. Point sources are selected from the DOLPHOT catalogs which satisfy basic requirements on signal-to-noise, sharpness, and data quality. The positions of these point sources are used to create maps with the same pixel grid

as the PHANGS-HST DRZ images, containing values of 1’s corresponding to the DOLPHOT positions, and 0’s otherwise. The maps are then smoothed with Gaussian profiles with FWHM of 2^n pc for $n = 3, 4, 5, 6$ (i.e. 8, 16, 32, 64 pc), computed given the distance of the galaxy. Finally, a high-pass filter is applied by subtracting a map that has been smoothed with a kernel which is four times larger.

K. Larson et al. then define two parameters which are tied to the characteristics of a single object on these smoothed, filtered positional maps. The peak threshold parameter is the level above which markers (local maxima) are identified; it is defined to be 1.5 times the maximum value for a single object so that the resulting regions are multi-peaked. The edge threshold parameter is the surface “brightness” level beyond which the regions are not allowed to expand further, and used to create a mask image for WATERSHED; it is defined to be the surface “brightness” at the FWHM of a single object.

The smoothed, filtered, positional maps enable the identification of structures on the physical scales over which the maps have been smoothed. The 8 pc smoothed maps allow associations that overlap in size with sources in the compact cluster catalog to be studied, and the maps smoothed over larger scales enable the greater star formation hierarchy to be traced. Structures are identified based on the NUV and V-band DOLPHOT point source catalogs. The resulting NUV-band selected association catalogs will predominantly contain young structures ($\lesssim 100$ Myr). In comparison, V-band selected catalogs will include structures over a full range of ages and will facilitate comparison with the compact cluster samples, which have also been V-band selected.

K. Larson et al. (in preparation) demonstrate the validity of this technique for identification of stellar associations in the PHANGS-HST galaxy sample based on analysis of NGC 3351 and NGC 1566.

Figure 9 shows the watershed identified stellar associations in NGC 3351 together with visually classified objects from the compact star cluster and association pipeline (Section 4.4). Three different magnifications of the galaxy are shown to illustrate the full disk and star-forming ring (bottom panels), the multi-scale associations traced by the watershed method (top left and middle panels), and individual compact star clusters and associations (series of postage stamps at top right). The structures are overlaid on color composites of the HST imaging, ALMA CO(2–1) map, and a color composite of the $H\alpha$ and $[\text{NII}]\lambda 6583$ maps from MUSE. Only the youngest (< 10 Myr) watershed associations are shown to illustrate the correlation with the blue star light,

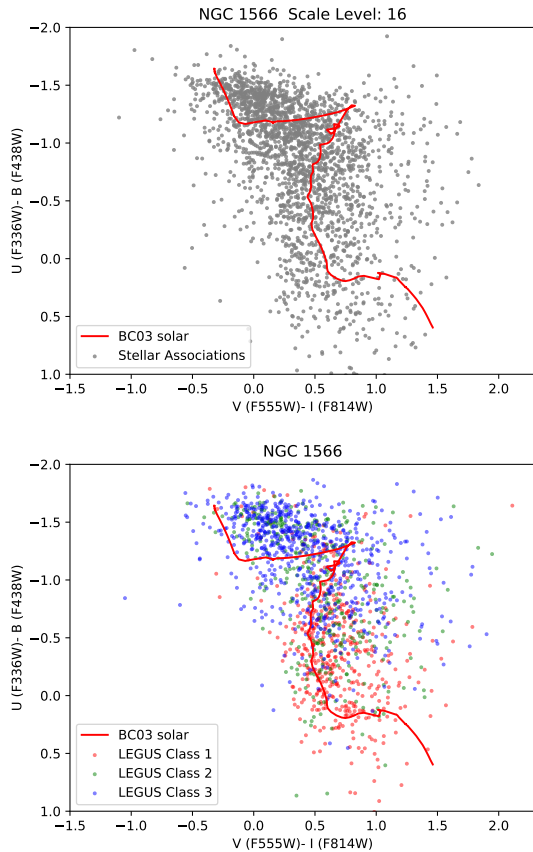


Figure 10. Comparison of UBVI color-color diagrams for multi-peak stellar associations identified with the PHANGS-HST watershed-based procedure (top panel), and compact star clusters and associations from the LEGUS program (bottom panel). The stellar associations are based on a V-band map of point source positions smoothed with a 16 pc FWHM gaussian kernel.

molecular clouds, and HII regions. Ages are derived using CIGALE as summarized in Section 4.6 and discussed in detail in Turner et al. (2021), and details on the procedures used to measure fluxes in the regions are presented in K. Larson et al. (in preparation).

From examination of the properties of the resultant watershed structures, we find:

- sample sizes of several hundred up to a few thousand associations in each galaxy. For associations identified on physical scales comparable to the aperture sizes used for selecting compact clusters candidates (4 pixel radius, which corresponds to 8 pc at a distance of 10 Mpc; Section 4.4), the numbers of associations identified are about $\sim 2-4$ times larger than the numbers of compact clusters, which have been visually classified;

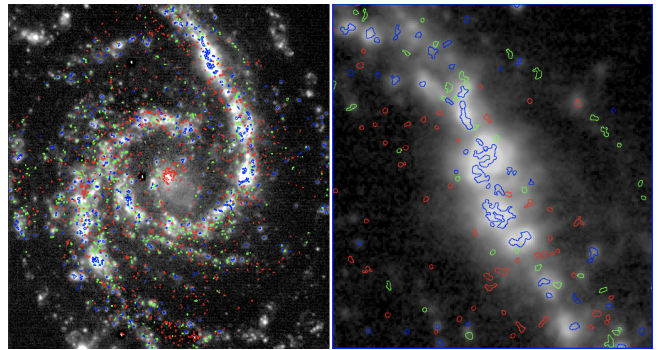


Figure 11. Stellar associations overlaid on PHANGS ground-based H α narrow band imaging for NGC 1566 (A. Razza et al. in preparation), color-coded by SED-fit age (1–3 Myr: blue, 3–5 Myr: green, >60 Myr red). Stellar associations have been identified from a V-band map of point source positions smoothed with a 32 pc FWHM gaussian kernel, and SED fitting performed with CIGALE assuming a single-aged stellar population. The right panel shows an expanded view of the northern spiral arm.

- the process is shown to successfully identify structures at the defined scale; the size distributions are well-defined, and approximately log-normal with medians near the FWHM of the smoothing kernel;
- fluxes computed within the boundaries of regions identified on the 8 and 16 pc smoothed images yield colors that are consistent with single-aged stellar population tracks on the UBVI color-color diagram. The loci are similar to samples of compact star cluster and associations (Figure 10);
- maps of the youngest associations (<5 Myr), show excellent correspondence to HII regions observed in narrowband H α imaging. As the age of the regions increases, they become more anti-correlated with the HII regions, as would be expected (Figure 11).

5. DATA PRODUCTS

The PHANGS-HST dataset will enable science extending well beyond the primary goals of the PHANGS collaboration. To enable the research community to make full use of the PHANGS-HST data, high-level science products from our star cluster and association catalog pipeline will be released. The following will be available through the PHANGS homepage at Mikulski Archive for Space Telescopes (MAST)¹³ with digital object identifier [DATASET].

¹³ <https://archive.stsci.edu/hlsp/phangs-hst/>

5.1. *Imaging*

For imaging of the star-forming disk in NUV-U-B-V-I bands for the 38 PHANGS-HST galaxies:

- FLC FITS file for each exposure with astrometric solutions updated based on GAIA DR2 sources.
- Combined DRC FITS images of individual pointings in each filter, each drizzled onto a common pixel grid defined for the galaxy target, also with astrometric solutions based on calibration to GAIA DR2 sources.
- Mosaicked DRC FITS images in each filter for 13 galaxies covered by multiple pointings (NGC 628, NGC 1097, NGC 1300, NGC 1512, NGC 1672, NGC 2903, NGC 3351, NGC 3621, NGC 3627, NGC 4254, NGC 4321, NGC 4536, NGC 6744).
- ERR and EXP weight FITS images for individual pointings as well as mosaics.

5.2. *Catalogs*

- DOLPHOT catalogs with 5-band PSF-fitting photometry.
- Compact star cluster and stellar association candidate catalogs, including position, 5-band aperture photometry, stellar mass, age, reddening, convolutional neural network morphological classification, visual classifications for a subset of candidates in the empirical selection region, multiple concentration indices (MCI) and standard concentration index (CI) values.
- Catalogs of stellar associations detected at 8, 16, 32, and 64 pc scales, including 5-band region photometry, stellar mass, age, reddening, effective radius, together with DS9 region files providing peak position and boundaries of regions, and FITS masks of regions.

5.3. *Software*

- The python routines that constitute the PHANGS-HST compact star cluster and association pipeline will be released at <https://github.com/PhangsTeam>.
- CIGALE augmentations for SED fitting of single-age stellar populations are available in dedicated branches, `SSP` and `SSPmag`, respectively, of the public `git` repository¹⁴ of CIGALE.

¹⁴ <https://gitlab.lam.fr/cigale/cigale.git>

- Convolutional neural network models for cluster candidate classification as described in Wei et al. (2020) and B. Whitmore et al. (in preparation). An annotated python notebook containing scripts to run the models will be provided. Future updates shown to be improvements over the current models will be released as they are developed.

5.4. *ALMA CO and MUSE Data*

PHANGS-ALMA data will be released for the full PHANGS parent sample through the ALMA Archive, the Canadian Astronomy Data Centre (CADC), and also linked to the PHANGS portal at MAST for those galaxies observed with HST. The PHANGS-ALMA products include the ¹²CO(2–1) spectral-line data cubes, signal masks, and derived products such as the integrated intensity, line-of-sight velocity estimate, and spectral line widths. A description of the data reduction and products is in Leroy et al. (2021), and the data release is discussed in A. K. Leroy et al. (in preparation).

Likewise, PHANGS-MUSE data of the 19 galaxies targeted in the course of that VLT Large Programme (ESO 1100.B-0651) will be released via the ESO Science Archive (<http://archive.eso.org/scienceportal/home>), CADC, and the PHANGS portal at MAST. The released MUSE data will include reduced and fully mosaicked datacubes as well as a series of two-dimensional maps associated with the gas and stellar tracers: broadband reconstructed images, emission line distribution and kinematics, stellar kinematics, star formation histories (mass and light-weighted age and metallicity maps), extinction maps from Balmer decrement and stellar continuum fitting. The details of the data reduction and analysis processes are provided in E. Emsellem et al. (in preparation).

Links to the archive locations for all released PHANGS products are available at the survey webpage (<http://phangs.org/data>).

6. SUMMARY

For decades, investigations of extragalactic molecular cloud and young resolved stellar populations have proceeded independently, and integrated analysis has been performed only for case studies of select nearby galaxies. With the transformative capabilities of ALMA and HST working in concert, PHANGS will help bridge the fields of star formation and galaxy evolution by investigating how small-scale physics, which create the basic quanta of star formation, may depend on the physical conditions of the greater galactic environment and conspire to produce galaxy scaling relationships.

With five band NUV-U-B-V-I imaging of the disks of 38 spiral galaxies at distances of 4–23 Mpc, and parallel V and I band imaging of their halos, PHANGS-HST will provide a census of tens of thousands of compact star clusters and associations, which will be combined with PHANGS-ALMA giant molecular clouds (and PHANGS-MUSE HII regions for 19 galaxies in the sample). Previous to this program, no HST wide-field UV imaging existed for 80% of the PHANGS-HST sample, and 60% did not have optical imaging with either WFC3 or ACS. Thus, PHANGS-HST provides a critical augmentation to the HST archive for nearby spiral galaxies in which both star clusters and molecular clouds can be efficiently detected by HST and ALMA over galactic scales. Altogether, PHANGS will provide an unprecedented joint catalog of the observed and physical parameters for $\sim 100,000$ star cluster, associations, HII regions, and molecular clouds.

In this paper, we have described the ensemble global properties of the 38 galaxy sample targeted for HST observations, and how they were selected from the parent PHANGS sample of nearby massive galaxies on the star-forming main sequence. The acquisition and processing of the HST observations to produce aligned, drizzled, science-ready images were described in detail. An overview of the major components of the pipeline developed to produce catalogs of single-peak compact star clusters, and a parallel pipeline for multi-scale stellar associations, was provided as a framework for forthcoming detailed papers on each of those components. We highlight new methods involving multiple concentration index (MCI) parameters, synthetic star clusters, and convolutional neural network models for cluster candidate selection and morphological classifications, as well as a watershed algorithm based procedure for identifying stellar associations from smoothed, filtered maps of point source positions. Data products to be released via MAST at <https://archive.stsci.edu/hlsp/phangs-hst/>, including imaging, catalogs, and software, were summarized, and will be useful for community science beyond the main goals of PHANGS.

These data products and the PHANGS census of star clusters, associations, HII regions and molecular clouds will provide context needed for meaningful study of the earliest phases of dust enshrouded star formation and ISM physics with JWST. Molecular clouds and UV bright clusters/associations are the precursors and descendants of the youngest dusty clusters in nearby galaxies to be studied in the infrared with JWST. With HST-matched resolution in the near-IR (PSF FWHM $0''.066$ at $2 \mu\text{m}$) and order-of-magnitude improved resolution compared to Spitzer in the mid-IR (PSF FWHM

of $0''.665$ at $21 \mu\text{m}$), molecular clouds with embedded sources can be identified, enabling a key test of our census of inactive clouds, and measurement of time to star formation onset. We will calculate mass functions, and spatial distributions for these sources, study their relation to those of other populations, and more clearly identify the conditions that ignite star formation. The combination of uniform, systematic observations from JWST combined with those already in hand from HST, ALMA, and VLT/MUSE will complete our understanding of the multi-scale process of star formation, and the progression from clouds to visible stars in a galactic context.

ACKNOWLEDGEMENTS

Based on observations made with the NASA/ESA Hubble Space Telescope, obtained from the data archive at the Space Telescope Science Institute. STScI is operated by the Association of Universities for Research in Astronomy, Inc. under NASA contract NAS 5-26555. Support for Program number 15654 was provided through a grant from the STScI under NASA contract NAS5-26555.

JCL acknowledges the W.M. Keck Institute for Space Studies (KISS) for its support of PHANGS-HST collaboration meetings where key work for this paper was performed. The PHANGS-HST survey benefited from discussions at the 2014 KISS workshop, “Bridging the Gap: Observations and Theory of Star Formation Meet on Large and Small Scales.”

JMDK and MC gratefully acknowledge funding from the Deutsche Forschungsgemeinschaft (DFG, German Research Foundation) through an Emmy Noether Research Group (grant number KR4801/1-1) and the DFG Sachbeihilfe (grant number KR4801/2-1). JMDK gratefully acknowledges funding from the European Research Council (ERC) under the European Union’s Horizon 2020 research and innovation programme via the ERC Starting Grant MUSTANG (grant agreement number 714907).

FB acknowledges funding from the European Research Council (ERC) under the European Union’s Horizon 2020 research and innovation programme (grant agreement No.726384/Empire).

RSK and SCOG acknowledge financial support from the DFG via the collaborative research center (SFB 881, Project-ID 138713538) “The Milky Way System” (sub-projects A1, B1, B2, and B8). They also acknowledge subsidies from the Heidelberg Cluster of Excellence *STRUCTURES* in the framework of Germany’s Excellence Strategy (grant EXC-2181/1 - 390900948)

and funding from the ERC via the ERC Synergy Grant *ECOGAL* (grant 855130).

KK gratefully acknowledges funding from the German Research Foundation (DFG) in the form of an Emmy Noether Research Group (grant number KR4598/2-1, PI Kreckel).

TGW acknowledges funding from the European Research Council (ERC) under the European Union’s Horizon 2020 research and innovation programme (grant agreement No. 694343).

ER acknowledges the support of the Natural Sciences and Engineering Research Council of Canada (NSERC), funding reference number RGPIN-2017-03987.

This paper makes use of the following ALMA data, which have been processed as part of the PHANGS-ALMA survey:

ADS/JAO.ALMA#2012.1.00650.S
 ADS/JAO.ALMA#2013.1.01161.S
 ADS/JAO.ALMA#2015.1.00925.S
 ADS/JAO.ALMA#2015.1.00956.S
 ADS/JAO.ALMA#2017.1.00886.L

This research has made use of the NASA/IPAC Extragalactic Database (NED) which is operated by the Jet Propulsion Laboratory, California Institute of Technology, under contract with NASA.

REFERENCES

- Adamo, A., Kruijssen, J. M. D., Bastian, N., Silva-Villa, E., & Ryon, J. 2015, *MNRAS*, 452, 246, doi: [10.1093/mnras/stv1203](https://doi.org/10.1093/mnras/stv1203)
- Adamo, A., Ryon, J. E., Messa, M., et al. 2017, *ApJ*, 841, 131, doi: [10.3847/1538-4357/aa7132](https://doi.org/10.3847/1538-4357/aa7132)
- Adamo, A., Hollyhead, K., Messa, M., et al. 2020, *MNRAS*, 499, 3267, doi: [10.1093/mnras/staa2380](https://doi.org/10.1093/mnras/staa2380)
- Anand, G. S., Rizzi, L., & Tully, R. B. 2018, *AJ*, 156, 105, doi: [10.3847/1538-3881/aad3b2](https://doi.org/10.3847/1538-3881/aad3b2)
- Anand, G. S., Lee, J. C., Van Dyk, S. D., et al. 2020, *MNRAS*, doi: [10.1093/mnras/staa3668](https://doi.org/10.1093/mnras/staa3668)
- Armus, L., Mazzarella, J. M., Evans, A. S., et al. 2009, *PASP*, 121, 559, doi: [10.1086/600092](https://doi.org/10.1086/600092)
- Barbarino, C., Dall’Ora, M., Botticella, M. T., et al. 2015, *MNRAS*, 448, 2312, doi: [10.1093/mnras/stv106](https://doi.org/10.1093/mnras/stv106)
- Blitz, L. 1993, in *Protostars and Planets III*, ed. E. H. Levy & J. I. Lunine, 125
- Boquien, M., Burgarella, D., Roehlly, Y., et al. 2019, *A&A*, 622, A103, doi: [10.1051/0004-6361/201834156](https://doi.org/10.1051/0004-6361/201834156)
- Bruzual, G., & Charlot, S. 2003, *MNRAS*, 344, 1000, doi: [10.1046/j.1365-8711.2003.06897.x](https://doi.org/10.1046/j.1365-8711.2003.06897.x)
- Burgarella, D., Buat, V., & Iglesias-Páramo, J. 2005, *MNRAS*, 360, 1413, doi: [10.1111/j.1365-2966.2005.09131.x](https://doi.org/10.1111/j.1365-2966.2005.09131.x)
- Calzetti, D., Johnson, K. E., Adamo, A., et al. 2015, *ApJ*, 811, 75, doi: [10.1088/0004-637X/811/2/75](https://doi.org/10.1088/0004-637X/811/2/75)
- Cardelli, J. A., Clayton, G. C., & Mathis, J. S. 1989, *ApJ*, 345, 245, doi: [10.1086/167900](https://doi.org/10.1086/167900)
- Chabrier, G. 2003, *PASP*, 115, 763, doi: [10.1086/376392](https://doi.org/10.1086/376392)
- Chandar, R., Fall, S. M., & Whitmore, B. C. 2010, *ApJ*, 711, 1263, doi: [10.1088/0004-637X/711/2/1263](https://doi.org/10.1088/0004-637X/711/2/1263)
- Chandar, R., Fall, S. M., Whitmore, B. C., & Mulia, A. J. 2017, *ApJ*, 849, 128, doi: [10.3847/1538-4357/aa92ce](https://doi.org/10.3847/1538-4357/aa92ce)
- Chevance, M., Kruijssen, J. M. D., Vazquez-Semadeni, E., et al. 2020, *SSRv*, 216, 50, doi: [10.1007/s11214-020-00674-x](https://doi.org/10.1007/s11214-020-00674-x)
- Cignoni, M., Sacchi, E., Aloisi, A., et al. 2018, *ApJ*, 856, 62, doi: [10.3847/1538-4357/aab041](https://doi.org/10.3847/1538-4357/aab041)
- Cignoni, M., Sacchi, E., Tosi, M., et al. 2019, *ApJ*, 887, 112, doi: [10.3847/1538-4357/ab53d5](https://doi.org/10.3847/1538-4357/ab53d5)
- Cook, D. O., Lee, J. C., Adamo, A., et al. 2019, *MNRAS*, 484, 4897, doi: [10.1093/mnras/stz331](https://doi.org/10.1093/mnras/stz331)
- Dobbs, C. L. 2008, *MNRAS*, 391, 844, doi: [10.1111/j.1365-2966.2008.13939.x](https://doi.org/10.1111/j.1365-2966.2008.13939.x)
- Dobbs, C. L., Bonnell, I. A., & Pringle, J. E. 2006, *MNRAS*, 371, 1663, doi: [10.1111/j.1365-2966.2006.10794.x](https://doi.org/10.1111/j.1365-2966.2006.10794.x)
- Dobbs, C. L., Krumholz, M. R., Ballesteros-Paredes, J., et al. 2014, in *Protostars and Planets VI*, ed. H. Beuther, R. S. Klessen, C. P. Dullemond, & T. Henning, 3, doi: [10.2458/azu_uapress_9780816531240-ch001](https://doi.org/10.2458/azu_uapress_9780816531240-ch001)
- Dolphin, A. E. 2002, *MNRAS*, 332, 91, doi: [10.1046/j.1365-8711.2002.05271.x](https://doi.org/10.1046/j.1365-8711.2002.05271.x)
- Elmegreen, B. G. 2000, *ApJ*, 530, 277, doi: [10.1086/308361](https://doi.org/10.1086/308361)
- . 2008, *ApJ*, 672, 1006, doi: [10.1086/523791](https://doi.org/10.1086/523791)
- Federrath, C. 2013, *MNRAS*, 436, 3167, doi: [10.1093/mnras/stt1799](https://doi.org/10.1093/mnras/stt1799)
- Freedman, W. L., Madore, B. F., Gibson, B. K., et al. 2001, *ApJ*, 553, 47, doi: [10.1086/320638](https://doi.org/10.1086/320638)
- Gaia Collaboration, Brown, A. G. A., Vallenari, A., et al. 2018, *A&A*, 616, A1, doi: [10.1051/0004-6361/201833051](https://doi.org/10.1051/0004-6361/201833051)
- Gieles, M., & Portegies Zwart, S. F. 2011, *MNRAS*, 410, L6, doi: [10.1111/j.1745-3933.2010.00967.x](https://doi.org/10.1111/j.1745-3933.2010.00967.x)
- Girichidis, P., Offner, S. S. R., Kritsuk, A. G., et al. 2020, *SSRv*, 216, 68, doi: [10.1007/s11214-020-00693-8](https://doi.org/10.1007/s11214-020-00693-8)
- Gnedin, N. Y. 2016, *Saas-Fee Advanced Course*, 43, 1, doi: [10.1007/978-3-662-47890-5_1](https://doi.org/10.1007/978-3-662-47890-5_1)

- Grasha, K., Calzetti, D., Adamo, A., et al. 2019, *MNRAS*, 483, 4707, doi: [10.1093/mnras/sty3424](https://doi.org/10.1093/mnras/sty3424)
- Haan, S., Surace, J. A., Armus, L., et al. 2011, *AJ*, 141, 100, doi: [10.1088/0004-6256/141/3/100](https://doi.org/10.1088/0004-6256/141/3/100)
- Hennebelle, P., & Falgarone, E. 2012, *A&A Rv*, 20, 55, doi: [10.1007/s00159-012-0055-y](https://doi.org/10.1007/s00159-012-0055-y)
- Heyer, M., & Dame, T. M. 2015, *ARA&A*, 53, 583, doi: [10.1146/annurev-astro-082214-122324](https://doi.org/10.1146/annurev-astro-082214-122324)
- Ho, I. T., Kreckel, K., Meidt, S. E., et al. 2019, *ApJL*, 885, L31, doi: [10.3847/2041-8213/ab4feb](https://doi.org/10.3847/2041-8213/ab4feb)
- Hopkins, P. F., Kereš, D., Oñorbe, J., et al. 2014, *MNRAS*, 445, 581, doi: [10.1093/mnras/stu1738](https://doi.org/10.1093/mnras/stu1738)
- Huang, C. D., Riess, A. G., Yuan, W., et al. 2020, *ApJ*, 889, 5, doi: [10.3847/1538-4357/ab5dbd](https://doi.org/10.3847/1538-4357/ab5dbd)
- Humphreys, R. M., & Davidson, K. 1979, *ApJ*, 232, 409, doi: [10.1086/157301](https://doi.org/10.1086/157301)
- Jacobs, B. A., Rizzi, L., Tully, R. B., et al. 2009, *AJ*, 138, 332, doi: [10.1088/0004-6256/138/2/332](https://doi.org/10.1088/0004-6256/138/2/332)
- Johnson, L. C., Seth, A. C., Dalcanton, J. J., et al. 2015, *ApJ*, 802, 127, doi: [10.1088/0004-637X/802/2/127](https://doi.org/10.1088/0004-637X/802/2/127)
- . 2016, *ApJ*, 827, 33, doi: [10.3847/0004-637X/827/1/33](https://doi.org/10.3847/0004-637X/827/1/33)
- Karachentsev, I. D., Karachentseva, V. E., Huchtmeier, W. K., & Makarov, D. I. 2004, *AJ*, 127, 2031, doi: [10.1086/382905](https://doi.org/10.1086/382905)
- Kennicutt, Jr., R. C. 1998, *ARA&A*, 36, 189, doi: [10.1146/annurev.astro.36.1.189](https://doi.org/10.1146/annurev.astro.36.1.189)
- Kim, D. C., Evans, A. S., Vavilkin, T., et al. 2013, *ApJ*, 768, 102, doi: [10.1088/0004-637X/768/2/102](https://doi.org/10.1088/0004-637X/768/2/102)
- Klessen, R. S., & Glover, S. C. O. 2016, *Saas-Fee Advanced Course*, 43, 85, doi: [10.1007/978-3-662-47890-5_2](https://doi.org/10.1007/978-3-662-47890-5_2)
- Kourkchi, E., Courtois, H. M., Graziani, R., et al. 2020, *AJ*, 159, 67, doi: [10.3847/1538-3881/ab620e](https://doi.org/10.3847/1538-3881/ab620e)
- Kourkchi, E., & Tully, R. B. 2017, *ApJ*, 843, 16, doi: [10.3847/1538-4357/aa76db](https://doi.org/10.3847/1538-4357/aa76db)
- Kreckel, K., Faesi, C., Kruijssen, J. M. D., et al. 2018, *ApJL*, 863, L21, doi: [10.3847/2041-8213/aad77d](https://doi.org/10.3847/2041-8213/aad77d)
- Kreckel, K., Ho, I. T., Blanc, G. A., et al. 2019, *ApJ*, 887, 80, doi: [10.3847/1538-4357/ab5115](https://doi.org/10.3847/1538-4357/ab5115)
- . 2020, *MNRAS*, 499, 193, doi: [10.1093/mnras/staa2743](https://doi.org/10.1093/mnras/staa2743)
- Kruijssen, J. M. D. 2012, *MNRAS*, 426, 3008, doi: [10.1111/j.1365-2966.2012.21923.x](https://doi.org/10.1111/j.1365-2966.2012.21923.x)
- Krumholz, M. R., & McKee, C. F. 2005, *ApJ*, 630, 250, doi: [10.1086/431734](https://doi.org/10.1086/431734)
- Krumholz, M. R., McKee, C. F., & Bland-Hawthorn, J. 2019, *ARA&A*, 57, 227, doi: [10.1146/annurev-astro-091918-104430](https://doi.org/10.1146/annurev-astro-091918-104430)
- Lada, C. J., & Lada, E. A. 2003, *ARA&A*, 41, 57, doi: [10.1146/annurev.astro.41.011802.094844](https://doi.org/10.1146/annurev.astro.41.011802.094844)
- Lamers, H. J. G. L. M., & Levesque, E. M. 2017, *Understanding Stellar Evolution*, doi: [10.1088/978-0-7503-1278-3](https://doi.org/10.1088/978-0-7503-1278-3)
- Larson, K. L., Díaz-Santos, T., Armus, L., et al. 2020, *ApJ*, 888, 92, doi: [10.3847/1538-4357/ab5dc3](https://doi.org/10.3847/1538-4357/ab5dc3)
- Leonard, D. C., Kanbur, S. M., Ngeow, C. C., & Tanvir, N. R. 2003, *ApJ*, 594, 247, doi: [10.1086/376831](https://doi.org/10.1086/376831)
- Leroy, A., Lee, J., Leroy, A., et al. 2021
- Leroy, A. K., Walter, F., Brinks, E., et al. 2008, *AJ*, 136, 2782, doi: [10.1088/0004-6256/136/6/2782](https://doi.org/10.1088/0004-6256/136/6/2782)
- Leroy, A. K., Walter, F., Sandstrom, K., et al. 2013, *AJ*, 146, 19, doi: [10.1088/0004-6256/146/2/19](https://doi.org/10.1088/0004-6256/146/2/19)
- Leroy, A. K., Sandstrom, K. M., Lang, D., et al. 2019, *ApJS*, 244, 24, doi: [10.3847/1538-4365/ab3925](https://doi.org/10.3847/1538-4365/ab3925)
- Lindegren, L., Hernández, J., Bombrun, A., et al. 2018, *A&A*, 616, A2, doi: [10.1051/0004-6361/201832727](https://doi.org/10.1051/0004-6361/201832727)
- Linden, S. T., Evans, A. S., Rich, J., et al. 2017, *ApJ*, 843, 91, doi: [10.3847/1538-4357/aa7266](https://doi.org/10.3847/1538-4357/aa7266)
- Lopez, L. A., Krumholz, M. R., Bolatto, A. D., et al. 2014, *ApJ*, 795, 121, doi: [10.1088/0004-637X/795/2/121](https://doi.org/10.1088/0004-637X/795/2/121)
- Mac Low, M.-M., & Klessen, R. S. 2004, *Reviews of Modern Physics*, 76, 125, doi: [10.1103/RevModPhys.76.125](https://doi.org/10.1103/RevModPhys.76.125)
- McKee, C. F., & Ostriker, E. C. 2007, *ARA&A*, 45, 565, doi: [10.1146/annurev.astro.45.051806.110602](https://doi.org/10.1146/annurev.astro.45.051806.110602)
- McQuinn, K. B. W., Skillman, E. D., Dolphin, A. E., Berg, D., & Kennicutt, R. 2017, *AJ*, 154, 51, doi: [10.3847/1538-3881/aa7aad](https://doi.org/10.3847/1538-3881/aa7aad)
- Meidt, S. E., Schinnerer, E., García-Burillo, S., et al. 2013, *ApJ*, 779, 45, doi: [10.1088/0004-637X/779/1/45](https://doi.org/10.1088/0004-637X/779/1/45)
- Meidt, S. E., Glover, S. C. O., Kruijssen, J. M. D., et al. 2020, *ApJ*, 892, 73, doi: [10.3847/1538-4357/ab7000](https://doi.org/10.3847/1538-4357/ab7000)
- Messa, M., Adamo, A., Östlin, G., et al. 2018, *MNRAS*, 473, 996, doi: [10.1093/mnras/stx2403](https://doi.org/10.1093/mnras/stx2403)
- Miville-Deschênes, M.-A., Murray, N., & Lee, E. J. 2017, *ApJ*, 834, 57, doi: [10.3847/1538-4357/834/1/57](https://doi.org/10.3847/1538-4357/834/1/57)
- Moffat, A. F. J. 1969, *A&A*, 3, 455
- Noll, S., Burgarella, D., Giovannoli, E., et al. 2009, *A&A*, 507, 1793, doi: [10.1051/0004-6361/200912497](https://doi.org/10.1051/0004-6361/200912497)
- Nugent, P., Sullivan, M., Ellis, R., et al. 2006, *ApJ*, 645, 841, doi: [10.1086/504413](https://doi.org/10.1086/504413)
- Olivares E., F., Hamuy, M., Pignata, G., et al. 2010, *ApJ*, 715, 833, doi: [10.1088/0004-637X/715/2/833](https://doi.org/10.1088/0004-637X/715/2/833)
- Olivier, G. M., Lopez, L. A., Rosen, A. L., et al. 2020, *arXiv e-prints*, arXiv:2009.10079. <https://arxiv.org/abs/2009.10079>
- Perez, G., Messa, M., Calzetti, D., et al. 2020, *arXiv e-prints*, arXiv:2012.09327. <https://arxiv.org/abs/2012.09327>
- Péroux, C., & Howk, J. C. 2020, *ARA&A*, 58, 363, doi: [10.1146/annurev-astro-021820-120014](https://doi.org/10.1146/annurev-astro-021820-120014)

- Pierce, M. J., Welch, D. L., McClure, R. D., et al. 1994, *Nature*, 371, 385, doi: [10.1038/371385a0](https://doi.org/10.1038/371385a0)
- Portegies Zwart, S. F., McMillan, S. L. W., & Gieles, M. 2010, *ARA&A*, 48, 431, doi: [10.1146/annurev-astro-081309-130834](https://doi.org/10.1146/annurev-astro-081309-130834)
- Rahner, D., Pellegrini, E. W., Glover, S. C. O., & Klessen, R. S. 2017, *MNRAS*, 470, 4453, doi: [10.1093/mnras/stx1532](https://doi.org/10.1093/mnras/stx1532)
- Reid, M. J., Pesce, D. W., & Riess, A. G. 2019, *ApJL*, 886, L27, doi: [10.3847/2041-8213/ab552d](https://doi.org/10.3847/2041-8213/ab552d)
- Ruiz-Lapuente, P. 1996, *ApJL*, 465, L83, doi: [10.1086/310155](https://doi.org/10.1086/310155)
- Ryon, J. E., Gallagher, J. S., Smith, L. J., et al. 2017, *ApJ*, 841, 92, doi: [10.3847/1538-4357/aa719e](https://doi.org/10.3847/1538-4357/aa719e)
- Sacchi, E., Cignoni, M., Aloisi, A., et al. 2018, *ApJ*, 857, 63, doi: [10.3847/1538-4357/aab844](https://doi.org/10.3847/1538-4357/aab844)
- Saintonge, A., Catinella, B., Tacconi, L. J., et al. 2017, *ApJS*, 233, 22, doi: [10.3847/1538-4365/aa97e0](https://doi.org/10.3847/1538-4365/aa97e0)
- Salim, S., Boquien, M., & Lee, J. C. 2018, *ApJ*, 859, 11, doi: [10.3847/1538-4357/aabf3c](https://doi.org/10.3847/1538-4357/aabf3c)
- Salim, S., Rich, R. M., Charlot, S., et al. 2007, *ApJS*, 173, 267, doi: [10.1086/519218](https://doi.org/10.1086/519218)
- Salim, S., Lee, J. C., Janowiecki, S., et al. 2016, *ApJS*, 227, 2, doi: [10.3847/0067-0049/227/1/2](https://doi.org/10.3847/0067-0049/227/1/2)
- Shaya, E. J., Tully, R. B., Hoffman, Y., & Pomarède, D. 2017, *ApJ*, 850, 207, doi: [10.3847/1538-4357/aa9525](https://doi.org/10.3847/1538-4357/aa9525)
- Sun, J., Leroy, A. K., Schruba, A., et al. 2018, *ApJ*, 860, 172, doi: [10.3847/1538-4357/aac326](https://doi.org/10.3847/1538-4357/aac326)
- Tonry, J. L., Dressler, A., Blakeslee, J. P., et al. 2001, *ApJ*, 546, 681, doi: [10.1086/318301](https://doi.org/10.1086/318301)
- Tully, R. B., Courtois, H. M., & Sorce, J. G. 2016, *AJ*, 152, 50, doi: [10.3847/0004-6256/152/2/50](https://doi.org/10.3847/0004-6256/152/2/50)
- Turner, J. A., Dale, D. A., Lee, J. C., et al. 2021, arXiv e-prints, arXiv:2101.02134, <https://arxiv.org/abs/2101.02134>
- van der Walt, S., Schönberger, J. L., Nunez-Iglesias, J., et al. 2014, arXiv e-prints, arXiv:1407.6245, <https://arxiv.org/abs/1407.6245>
- Walch, S., Girichidis, P., Naab, T., et al. 2015, *MNRAS*, 454, 238, doi: [10.1093/mnras/stv1975](https://doi.org/10.1093/mnras/stv1975)
- Ward, J. L., & Kruijssen, J. M. D. 2018, *MNRAS*, 475, 5659, doi: [10.1093/mnras/sty117](https://doi.org/10.1093/mnras/sty117)
- Ward, J. L., Kruijssen, J. M. D., & Rix, H.-W. 2020, *MNRAS*, 495, 663, doi: [10.1093/mnras/staa1056](https://doi.org/10.1093/mnras/staa1056)
- Wei, W., Huerta, E. A., Whitmore, B. C., et al. 2020, *MNRAS*, 493, 3178, doi: [10.1093/mnras/staa325](https://doi.org/10.1093/mnras/staa325)
- Whitmore, B. C., Chandar, R., & Fall, S. M. 2007, *AJ*, 133, 1067, doi: [10.1086/510288](https://doi.org/10.1086/510288)
- Whitmore, B. C., Zhang, Q., Leitherer, C., et al. 1999, *AJ*, 118, 1551, doi: [10.1086/301041](https://doi.org/10.1086/301041)
- Wright, N. J. 2020, *NewAR*, 90, 101549, doi: [10.1016/j.newar.2020.101549](https://doi.org/10.1016/j.newar.2020.101549)

Galaxy	α	δ	b	D	$\sigma(D)$	Method	$D(\text{Ref})$	i	T	SFR	$\log M_*$	Σ_{CO}
(1)	[J2000]	[J2000]	[deg]	[Mpc]	[Mpc]	(7)	(8)	[deg]	(10)	$[M_\odot \text{ yr}^{-1}]$	$[\log M_\odot]$	$[M_\odot \text{ kpc}^{-2}]$
	(2)	(3)	(4)	(5)	(6)			(9)		(11)	(12)	(13)
IC 1954	03h31m31.39s	-51d54m17.4s	-51.201	12.8	2.05	NAM+TF	3+4+5	57	3.3	0.3	9.6	1.1
IC 5332 ^M	23h34m27.49s	-36d06m03.9s	-71.366	9.01	0.41	TRGB	18	27	6.8	0.3	9.5	-999
NGC 628 ^M	01h36m41.75s	+15d47m01.2s	-45.705	9.84	0.63	TRGB	2	9	5.2	1.7	10.2	1.5
NGC 685	01h47m42.81s	-52d45m42.5s	-62.304	19.94	2.99	NAM	4+5	23	5.4	0.4	9.9	0.6
NGC 1087 ^M	02h46m25.16s	-00d29m55.1s	-51.651	15.85	2.24	Group	6	43	5.2	1.3	9.9	1.3
NGC 1097	02h46m19.05s	-30d16m29.6s	-64.681	13.58	2.04	NAM	4+5	49	3.3	4.6	10.7	2.2
NGC 1300 ^M	03h19m41.08s	-19d24m40.9s	-55.223	18.99	2.85	NAM	4+5	32	4	1.1	10.6	1.0
NGC 1317	03h22m44.29s	-37d06m13.3s	-56.693	19.11	0.84	Group	2	23	0.8	0.4	10.6	1.7
NGC 1365 ^M	03h33m36.37s	-36d08m25.4s	-54.598	19.57	0.78	TRGB	2	55	3.2	16.4	10.8	2.7
NGC 1385 ^M	03h37m28.85s	-24d30m01.1s	-52.706	17.22	2.58	NAM	4+5	44	5.9	2.0	9.9	1.3
NGC 1433 ^M	03h42m01.55s	-47d13m19.5s	-51.195	15.17	1.52	PNLF	7	29	1.5	0.4	10.4	1.3
NGC 1512 ^M	04h03m54.28s	-43d20m55.9s	-48.166	15.94	1.59	PNLF	7	43	1.2	0.8	10.6	1.1
NGC 1559	04h17m35.77s	-62d47m01.2s	-41.198	19.44	0.44	Mira	8	65	5.9	4.5	10.2	1.5
NGC 1566 ^M	04h20m00.42s	-54d56m16.1s	-43.393	17.69	2.00	Group	6	30	4	4.4	10.7	2.0
NGC 1672 ^M	04h45m42.50s	-59d14m49.9s	-38.990	19.40	2.91	NAM	4+5	43	3.3	7.4	10.6	2.1
NGC 1792	05h05m14.45s	-37d58m50.7s	-36.453	16.20	2.43	NAM	4+5	65	4	3.5	10.5	1.8
NGC 2775	09h10m20.12s	+07d02m16.6s	33.988	23.15	3.47	NAM	4+5	41	1.6	0.8	11.1	1.2
NGC 2835 ^M	09h17m52.91s	-22d21m16.8s	18.509	12.22	0.94	TRGB	18	41	5	1.2	9.8	0.9
NGC 2903	09h32m10.11s	+21d30m03.0s	44.540	10.0	2.5	NAM+TF	3+4+5	67	4	2.9	10.6	1.7
NGC 3351 ^M	10h43m57.70s	+11d42m13.7s	56.368	9.96	0.33	TRGB	2	45	3.1	1.2	10.3	1.4
NGC 3621	11h18m16.51s	-32d48m50.6s	26.099	7.06	0.28	TRGB	18	66	6.9	1.0	10.0	1.4
NGC 3627 ^M	11h20m14.96s	+12d59m29.5s	64.418	11.32	0.48	TRGB	2	57	3.1	3.7	10.7	1.9
NGC 4254 ^M	12h18m49.60s	+14d24m59.4s	75.190	13.1	2.8	SCM	14	34	5.2	3.0	10.3	2.2
NGC 4298	12h21m32.76s	+14d36m22.2s	75.673	14.92	1.37	TRGB	18	59	5.1	0.3	9.9	1.4
NGC 4303 ^M	12h21m54.90s	+04d28m25.1s	66.276	16.99	3.04	Group	6	24	4	5.1	10.6	2.1
NGC 4321 ^M	12h22m54.83s	+15d49m18.5s	76.898	15.21	0.49	Cepheid	10	39	4	3.5	10.7	1.6
NGC 4535 ^M	12h34m20.31s	+08d11m51.9s	70.641	15.77	0.37	Cepheid	10	45	5	2.0	10.5	1.2
NGC 4536	12h34m27.05s	+02d11m17.3s	64.730	16.25	1.13	TRGB	2	66	4.3	3.4	10.2	1.4
NGC 4548	12h35m26.45s	+14d29m46.8s	76.830	16.22	0.38	Cepheid	10	38	3.1	0.5	10.7	1.0
NGC 4569	12h36m49.79s	+13d09m46.6s	75.623	15.76	2.36	Group	6	70	2.4	1.3	10.8	1.4
NGC 4571	12h36m56.38s	+14d13m02.5s	76.654	14.9	1.2	Cepheid	16	33	6.4	0.3	10.0	0.9
NGC 4654	12h43m56.58s	+13d07m36.0s	75.889	21.98	1.16	Group	10	56	5.9	3.5	10.5	1.4
NGC 4689	12h47m45.56s	+13d45m46.1s	76.607	15.0	2.25	NAM+TF	3+4+5	39	4.7	0.4	10.1	0.9
NGC 4826	12h56m43.64s	+21d40m58.7s	84.423	4.41	0.19	TRGB	18	59	2.2	0.2	10.2	1.5
NGC 5068 ^M	13h18m54.81s	-21d02m20.8s	41.376	5.20	0.21	TRGB	18	36	6	0.3	9.4	0.8
NGC 5248	13h37m32.02s	+08d53m06.6s	68.751	14.87	1.34	Group	6	47	4	2.1	10.3	1.8
NGC 6744	19h09m46.10s	-63d51m27.1s	-26.146	9.39	0.43	TRGB	18	53	4	2.4	10.7	1.0
NGC 7496 ^M	23h09m47.29s	-43d25m40.6s	-63.801	18.72	2.81	NAM	4+5	36	3.2	2.1	9.8	1.2

Table 1. PHANGS-HST Galaxy Sample**Col 1:** Galaxy name. *M* denotes PHANGS-MUSE IFU spectroscopy available.**Col 2-3:** Right Ascension and Declination.**Col 4:** Galactic Latitude.**Col 5-8:** Galaxy distances, uncertainties, and references as follows:

1) Karachentsev et al. (2004) 2) Jacobs et al. (2009) 3) Tully et al. (2016) 4) Shaya et al. (2017) 5) Kourkchi et al. (2020) 6) Kourkchi & Tully (2017) 7) F. Scheuermann et al., in preparation 8) Huang et al. (2020) 9) Leonard et al. (2003) 10) Freedman et al. (2001) 11) Olivares E. et al. (2010) 12) Barbarino et al. (2015) 13) Tonry et al. (2001) 14) Nugent et al. (2006) 15) Reid et al. (2019) 16) Pierce et al. (1994) 17) Ruiz-Lapuente (1996) 18) Anand et al. (2020)

Col 9: Galaxy inclination. Following A.K. Leroy et al. (in preparation) and adopted from Lang et al. (2020).**Col 10:** Morphological T-type.**Col 11:** Star formation rate. Following A.K. Leroy et al. (in preparation), based on GALEX and WISE data with SFR prescription calibrated to match results from population synthesis modeling of (Salim et al. 2016, 2018).**Col 12:** Galaxy stellar mass. Following A.K. Leroy et al. (in preparation), based on Spitzer IRAC 3.6 μm when available, or WISE 3.4 μm , and mass-to-light ratio prescription of (Leroy et al. 2019) calculated as a function of radius in the galaxy.**Col 13:** Here we calculate Σ_{mol} adopting a fixed $\alpha_{\text{CO}}^{2-1} = 6.25 M_\odot \text{ pc}^{-2} (\text{K km s}^{-1})^{-1}$, appropriate for a Galactic conversion factor and a typical CO (2-1)/CO (1-0) line ratio (Sun et al. 2018). Thus, the *x*-axis indicates mean CO surface brightness in units of mass surface density.